Factors controlling landslide frequency–area distributions

Hakan Tanyaş,[1]* iD Cees J. van Westen,[1] iD Kate E. Allstadt[2] iD and Randall W. Jibson[2] iD
[1] Faculty of Geo-Information Science and Earth Observation (ITC), University of Twente, The Netherlands
[2] US Geological Survey, Geologic Hazards Science Center, Golden, Colorado USA

Earth Surface Processes and Landforms

ABSTRACT: A power-law relation for the frequency–area distribution (FAD) of medium and large landslides (e.g. tens to millions of square meters) has been observed by numerous authors. But the FAD of small landslides diverges from the power-law distribution, with a rollover point below which frequencies decrease for smaller landslides. Some studies conclude that this divergence is an artifact of unmapped small landslides due to lack of spatial or temporal resolution; others posit that it is caused by the change in the underlying failure process. An explanation for this dilemma is essential both to evaluate the factors controlling FADs of landslides and power-law scaling, which is a crucial factor regarding both landscape evolution and landslide hazard assessment. This study examines the FADs of 45 earthquake-induced landslide inventories from around the world in the context of the proposed explanations. We show that each inventory probably involves some combination of the proposed explanations, though not all explanations contribute to each case. We propose an alternative explanation to understand the reason for the divergence from a power-law. We suggest that the geometry of a landslide at the time of mapping reflects not just one single movement but many, including the propagation of numerous smaller landslides before and after the main failure. Because only the resulting combination of these landslides can be observed due to a lack of temporal resolution, many smaller landslides are not taken into account in the inventory. This reveals that the divergence from the power-law is not necessarily attributed to the incompleteness of an inventory. This conceptual model will need to be validated by ongoing observation and analysis. Also, we show that because of the subjectivity of mapping procedures, the total number of landslides and total landslide areas in inventories differ significantly, and therefore the shapes of FADs also differ considerably. © 2018 The Authors. Earth Surface Processes and Landforms published by John Wiley & Sons Ltd.

KEYWORDS: earthquakes; landslides; inventories; landslide size-statics; power-law; rollover; cutoff; amalgamation; temporal resolution; successive slope failure

Introduction

The statistical properties of landslide inventories are commonly described using frequency–area distribution (FAD) curves, which plot landslide areas versus the corresponding cumulative or non-cumulative landslide frequencies. Observations show that a power-law seems to be valid for medium and large landslides (e.g. tens to millions of square meters), and also for rock-fall distributions across the range of rock-fall sizes (Malamud *et al.*, 2004).

The slope of the power-law is defined using a power-law exponent (scaling parameter, β) (Figure 1). The power-law tail, where we calculate β, is arguably the most important part of the FAD because it gives insight to the characteristics of landslide size distribution and contains the greatest volume of material (Bennett *et al.*, 2012). For example, Hovius *et al.* (1997) used β to quantify total denudation caused by landsliding. Power-law fit and the identified β value also are used as a tool for quantitative analysis of landslide hazard (Guzzetti *et al.*, 2005). However, the β value of a given FAD is sensitive to

minor differences in the method used to estimate β (Bennett *et al.*, 2012; Tanyaş *et al.*, 2018). Additionally, other factors such as mapping techniques and expertise of mappers can cause uncertainty in FAD and β, which has not been analyzed in detail.

For most landslide inventories, the frequencies of small landslides generally diverge from the power-law (Guzzetti *et al.*, 2002; Malamud *et al.*, 2004; Stark and Hovius, 2001; Van Den Eeckhaut *et al.*, 2007). The point where divergence begins is defined as the cutoff point (Stark and Hovius, 2001) which is visible in both the cumulative and non-cumulative FADs (Figure 1). For non-cumulative landslide FADs, the peak point of the curve after which the frequency–density value begins to decrease for smaller landslides following a positive power-law decay is commonly referred to as the rollover point (Van Den Eeckhaut *et al.*, 2007) (Figure 1(a)). Some studies refer to the cutoff point as the rollover point (Parker *et al.*, 2015), but in this study, we refer to the divergence point as the cutoff point and the peak point of the non-cumulative probability distribution curve as the rollover point.
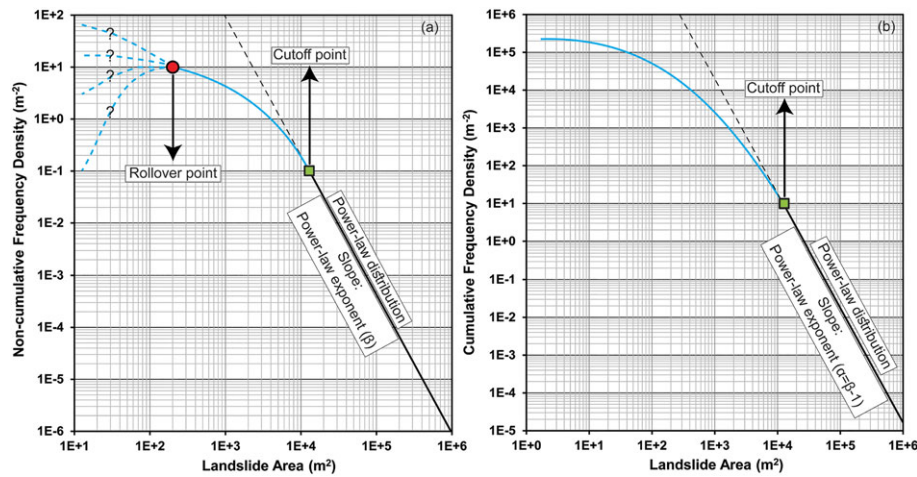
Figure 1. Schematic of the main components of a (a) non-cumulative, and (b) cumulative FAD of a landslide-event inventory. [Colour figure can be viewed at wileyonlinelibrary.com]

The cause of the divergence is a controversial issue and five hypotheses for this divergence have been proposed. The focus of this issue is the cutoff point rather than the rollover point (Figure 1) because that is where the divergence from the negative power-law decay is first observed.

The first hypothesis (*Hypothesis 1*) is that the power-law divergence is an artifact of undersampling small slides (Hungr *et al.*, 1999; Stark and Hovius, 2001; Brardinoni and Church, 2004) caused by inadequate resolution of the imagery used to create the landslide inventory.

Three other hypotheses (*Hypothesis 2, 3* and *4*) that argue that the divergence from the power-law is real and can be attributed to physical explanations. *Hypothesis 2* suggests that rollover is caused by the transition between the factors controlling slope-failure mechanisms of large, deep landslides versus small, shallow landslides (Katz and Aharonov, 2006). Guzzetti *et al.* (2002) argued that large, deep landslides are primarily controlled by friction, whereas small, shallow landslides are controlled more by cohesion. Stark and Guzzetti (2009) and Frattini and Crosta (2013) used the mechanical properties of the substrate to propose an explanation for the power-law divergence. Stark and Guzzetti (2009) claimed that the scaling of small, shallow failures is the result of the low cohesion of soil and regolith, whereas the power-law distribution observed for larger landslides is controlled by the greater cohesion of bedrock. Similarly, Bennett *et al.* (2012) suggest through analysis of a large database of landslides in the Illgraben, Switzerland, that failures within the rollover and power-law parts of the distribution represent two different types of slope failure. Type-1 refers to the numerous small, shallow slides within the top loose weathered layer of slopes where the depth and thus the size of the distribution is limited by the depth of the weathered layer. The depth of this layer limits the volume of landsliding and causes the rollover. Type-2 slides are less common, deeper and larger rock slides and falls where the depth is controlled by fractures within the bedrock. These failures have a wide range of depths and make up the power-law tail.

Hypothesis 3 is based on the geomorphology of an area and claims that the distribution of soil moisture over the landscape controls the size distribution and FADs of landslides (Pelletier *et al.*, 1997). To model the FAD of landslides, Pelletier *et al.* (1997) examined the FADs of two historical and one earthquake-induced landslide-event inventory and conducted a slope-stability analysis using soil moisture as a controlling factor. They defined the domains where shear stress is greater than a threshold value and showed that FADs of these domains give similar power-law to FADs of landslides. According to this hypothesis, the landslide areas could be associated with areas of simultaneously high levels of soil moisture and steep slopes. Whereas this might be the case for medium and large landslides, the terrain surface is not dissected on a scale that would control smaller landslides, and so fewer landslides in this size range are expected. Therefore, the effect of the smooth topography at small scales causes rollover in the FAD of landslides.

Hypothesis 4 posits that the power-law divergence results from physiographic limitations (Guthrie and Evans, 2004; Guthrie *et al.*, 2008). This argument suggests that middle and upper slopes are most susceptible to landslide initiation because of steepness, and the mobilized material moves downslope and amalgamates into larger landslides. Small landslides occur where long runout is improbable because of the physiography of the slope; such areas are less common in most landscapes. Thus, this argument interprets the power-law divergence as a consequence of slope-length constraint on the downslope propagation of long-runout landslides.

Hypothesis 5 suggests that a lack of temporal mapping resolution causes rollover observed in rock-falls (Williams *et al.*, 2018). Barlow *et al.* (2012) showed the effect of temporal resolution of mapping on FADs of rock-falls. They compared inventories having temporal resolutions of 1 and 19 months and stated that coarser temporal resolution causes an increase in the superimposition of rock-fall events. Williams *et al.* (2018) went one step further by monitoring rock-falls on a slope (length ~180 m and height ~60 m) at approximately 1-hour intervals. They showed that increasing temporal resolution captures many smaller failures and significantly changes the FAD. Williams *et al.* (2018) also showed that this high-temporal-resolution monitoring increased the power-law exponent to 2.27 (1 hour) from 1.78 (30 days). Additionally, they reported that the low-temporal-resolution inventory (30 days) had a rollover, whereas the inventory created from near-continuous slope monitoring did not.

There is currently no consensus on the reason why landslides show fractal size distributions and the FAD diverges from fractal scaling for small landslide areas. The arguments about whether the rollover is real or is an artifact can be traced back to the very definition of a landslide. The definition of what constitutes a single occurrence of a landslide can be complex and a matter of debate; this differs significantly from other phenomena that have a power-law relation, such as earthquakes. Earthquakes are recorded by seismometers and, except for events closely spaced in time, each distinct fault rupture can be assessed

and quantified separately from others. In this context, divergence from the power-law decay is attributed to the loss of perceptibility of smaller events (Davison and Scholz, 1985). When quantifying landslides, on the other hand, the number of landslides cannot be objectively identified because of both amalgamation of coalescing or adjacent landslides and the subjectivity of mapping procedures.

Several factors cause the amalgamation of landslides in inventory maps. Delineating landslide polygons is subjective and depends on the methodology followed, the skill of the interpreters, and the time invested in the inventory (Soeters and van Westen, 1996). Adjacent landslides commonly are delineated as a single polygon if their runouts or scars overlap and differentiation is difficult (Harp and Jibson, 1995, 1996). Poor image resolution or contrast between affected and unaffected areas might be another reason for amalgamation (Marc and Hovius, 2015). Lack of temporal resolution also can cause amalgamation of landslides.

Marc and Hovius (2015) propose a method for automatic detection and separation of amalgamated polygons. The algorithm redefines landslide polygons according to geometric and topographic considerations. For example, if a landslide polygon crosses a ridge, the algorithm splits this polygon into two along the ridge-line. The methodology provides only a partial correction for amalgamated landslides, however. Along the same slope, multiple adjacent landslides can be triggered and amalgamated. For such cases, the suggested methodology is not capable of detecting amalgamation.

Li *et al*. (2014) manually differentiate the amalgamated landslides provided by an automated landslide-detection algorithm (Parker *et al*., 2011) for the 2008 Wenchuan earthquake-induced landslide (EQIL) inventory. They show that amalgamated landslides can strongly bias both total number of landslides and individual landslide areas. As a result, this also significantly affects the FAD of landslides and the estimated landslide volume, which is highly sensitive to the changes both in the number of landslides and the area of each individual landslide (Li *et al*., 2014).

No clear physical process explains why landslide distributions should follow a power-law across the entire size distribution (Hergarten, 2003). Yet considering the literature showing that the power-law seems to be valid for medium and large landslides, it is logical to hypothesize that in the absence of artifacts, the scaling might also continue to smaller landslide sizes as is the case for rock fall inventories (Williams *et al*., 2018). If it does not, then a physical explanation should reveal something about the fundamentals of landslide processes. Whether the cutoff and rollovers are artifacts or if they reflect an actual change in the physical process for smaller slides is unclear. A consistent explanation for the observed variability in FAD patterns can help us isolate the physically based factors that yield a fundamental understanding of the landslide process. Explaining this issue also provides valuable information to understand the factors controlling the FAD of landslides and the power-law exponent (β) as well.

This study aims to better understand the factors controlling the FADs of landslides, particularly why the FAD cutoffs and rollovers are present even in inventories that are considered complete. We do so by analyzing 45 digital EQIL inventories triggered by 32 earthquakes. This contrasts with the aforementioned studies that base their proposed explanations only on one or a few inventories. We analyze the different proposed rollover explanations using examples from these data and show that though each could contribute in some way, none of them by itself is adequate to cover the whole phenomenon. We elaborate on the argument that lack of temporal resolution in mapping of landslides causes superimposition and

coalescence of features because the landslide events that happened at different times are formed on top of each other and afterwards look like a single event (Barlow *et al*., 2012; Williams *et al*., 2018). We suggest an alternative conceptual model to the existing hypotheses. Our model argues that the divergence from the power-law and rollover are caused by lack of temporal resolution with which to capture the smallest of landslides.

Input Data

Earlier studies for explaining the rollover use a variety of historical landslide inventories that are not limited to those related to earthquakes (Guzzetti *et al*., 2002; Malamud *et al*., 2004). We use an EQIL inventory database (Schmitt *et al*., 2017) that was collected by Tanyaş *et al*. (2017).

This database contains 64 digital EQIL inventory maps from around the world covering the period from 1971 to 2016. However, they have differing levels of quality and completeness because each inventory was created for a different purpose based on different expertise and materials. For example, the 2015 Gorkha EQIL inventory of Tanyaş *et al*. (2018) was created soon after the earthquake to understand the general spatial size-distribution characteristics of the triggered landslides; therefore, the inventory is preliminary and includes only a small part of the landslide-affected area with a high amount of amalgamation. On the other hand, Harp *et al*. (2016) published the 2010 Haiti inventory about six years after the event. This inventory covers the entire area affected by landslides down to the smallest resolvable landslide sizes and is far more detailed and comprehensive.

The 45 EQIL inventories from 32 earthquakes used in this study are described in Table I. Except for the 2008 Wenchuan inventory of Li *et al*. (2014) and the 2007 Pisco inventory of Lacroix *et al*. (2013), where landslides were mapped from satellite imagery using an automated algorithm and manual delineation, all other inventories were created primarily based on systematic visual interpretation of satellite images and/or aerial photography (Tanyaş *et al*., 2017).

Tanyaş *et al*. (2018) numerically assessed the validity of power-law distribution for these earthquake-induced landslide inventories. They used the method of Clauset *et al*. (2009) and generated *P*-values based on the Kolomogrov–Smirnov statistic. A *P*-value close to 1 indicates a good fit to the power-law distribution, whereas a p-value equal to or less than 0.1 might indicate that the power-law is not a plausible fit to the data. They showed that 39 of the 45 inventories have *P*-values larger than 0.1 and thus the power-law fit is a plausible hypothesis for landslide inventories in general.

Analysis

FADs of EQIL inventories

We calculate the cutoff and *P*-values using the method described by Clauset *et al*. (2009) (Table I) (see Supplementary material) and plotted the landslide FADs from the inventories analyzed (Figure 2). We identify the landslide size bin where the corresponding FAD begins to roll over. We consider them approximate rollover points (Table I) because the locations of rollover points differ slightly based on the binning methodology. We identify rollover points using ten different bin sizes to quantify the variation in rollover point (see Supplementary material). As a result, we define average rollover values with 95% confidence intervals. Empirical curves from Malamud *et al*.

Table I. EQIL inventories used in this study. Cutoff and *P*-values were determined using the methodology of Clauset *et al.* (2009)

ID	Location	Date/Time	*P*-value	β	Approximate rollover point (m^2)	Cutoff points (m^2)	Reference study
1	Guatemala	1976-02-04/09:01:43 UTC	0.67	2.21±0.14		19135±7×10^3	Harp *et al.*, 1981
2	Friuli (Italy)	1976-05-06/20:00:11 UTC	0.45	2.20±0.09	2050±211	1466±1×10^3	Govi, 1977
3	Izu Oshima Kinkai (Japan)	1978-01-14/03:24:39 UTC	0.89	2.61±0.11	537±83	1508±2×10^2	Suzuki, 1979
4	Mammoth Lakes (USA)	1980-05-25/19:44:50 UTC	0*	2.29±0.09	2696±467	6784±2×10^3	Harp *et al.*, 1984
5	Coalinga (USA)	1983-05-02/23:42:37 UTC	0.31	2.64±0.06		1831±3×10^2	Harp and Keefer, 1990
6	Loma Prieta, California (US)	1989-10-18/00:04:15 UTC	0.55	2.93±0.28		3642±5×10^2	McCrink, 2001
7	Limon (Costa Rica)	1991-04-22/21:56:51 UTC	0.92	3.30±0.18	1231±189	9171±1×10^3	Marc *et al.*, 2016
8	Finisterre Mt./ (Papua N. G.)	1993-10-13/02:06:00 UTC	0.96	2.40±0.18	2351±354	34585±9×10^3	Meunier *et al.*, 2008
9	Northridge (USA)	1994-01-17/12:30:55 UTC	0.88	2.62±0.11	617±74	9189±1×10^3	Harp and Jibson, 1995, 1996
10	Hyogo-ken Nanbu (Japan)	1995-01-16/20:46:52 UTC	0.11	2.17±0.02	66±8	102±2×10^0	Uchida *et al.*, 2004
11	Umbria-Marche (Italy)	1997-09-26/09:40:26 UTC	0.55	2.85±0.37	4461±461	10412±3×10^3	Marzorati *et al.*, 2002
12	Jueili (Taiwan)	1998-07-17/04:51:14 UTC	0.99	3.21±0.60	2168±378	10920±3×10^3	Huang and Lee, 1999
13	Chi-chi (Taiwan)	1999-09-20/17:47:18 UTC	0.99	2.29±0.09	881±138	26259±7×10^3	Liao and Lee, 2000
14	Denali Alaska	2002-11-03/22:12:41 UTC	0.96	2.11±0.06	16144±1997	24153±7×10^3	Gorum *et al.*, 2014
15	Lefkada Ionian Islands (Greece)	2003-08-14/05:14:54 UTC	0.83	2.77±0.46	1984±219	19164±8×10^3	Papathanassiou *et al.*, 2013
16a	Mid-Niigata (Japan)	2004-10-23/08:56:00 UTC	0.11	2.31±0.21	508±87	520±2×10^2	GSI of Japan, 2005
16b	Mid-Niigata (Japan)	2004-10-23/08:56:00 UTC	0.96	2.32±0.05	1198±207	1683±4×10^2	Sekiguchi and Sato, 2006
16c	Mid-Niigata (Japan)	2004-10-23/08:56:00 UTC	0.25	2.48±0.04	617±74	1157±2×10^1	Yagi *et al.*, 2007
17a	Kashmir (India-Pakistan)	2005-10-08/03:50:40 UTC	0.58	2.39±0.12	804±152	6573±1×10^3	Sato *et al.*, 2007
17b	Kashmir (India-Pakistan)	2005-10-08/03:50:40 UTC	0.76	2.39±0.07	4166±547	44139±5×10^3	Basharat *et al.*, 2014
17c	Kashmir (India-Pakistan)	2005-10-08/03:50:40 UTC	0.62	3.67±0.09	8767±1450	57717±9×10^3	Basharat *et al.*, 2016
18	Kiholo Bay (Hawaii)	2006-10-15/17:07:49 UTC	0.94	2.45±0.46		17203±6×10^3	Harp *et al.*, 2014
19a	Aysen Fjord (Chile)	2007-04-21/17:53:46 UTC	0.57	2.07±0.10	2115±527	19166±3×10^3	Sepúlveda *et al.*, 2010
19b	Aysen Fjord (Chile)	2007-04-21/17:53:46 UTC	0.01*	1.82±0.18	2578±512	5312±3×10^3	Gorum *et al.*, 2014
20	Niigata Chuetsu-Oki (Japan)	2007-07-16/01:13:22 UTC	0.80	2.80±0.28	1009±109	828±3×10^2	Kokusai Kogyo, 2007
21	Pisco (Peru)	2007-08-15/23:40:57 UTC	0.93	2.63±0.23	2080±332	4100±1×10^3	Lacroix *et al.*, 2013
22a	Wenchuan (China)	2008-05-12/06:28:01 UTC	0.12	2.77±0.10	1110±190	97846±1×10^4	Dai *et al.*, 2011
22b	Wenchuan (China)	2008-05-12/06:28:01 UTC	1.00	3.09±0.10	1110±190	143664±6×10^3	Xu *et al.*, 2014b
22c	Wenchuan (China)	2008-05-12/06:28:01 UTC	0*	3.23±0.05	1661±211	78826±5×10^3	Li *et al.*, 2014
22d	Wenchuan (China)	2008-05-12/06:28:01 UTC	1.00	2.72±0.12	357±67	39169±4×10^3	Tang *et al.*, 2016
23	Iwate–Miyagi Nairiku (Japan)	2008-06-13/23:43:45 UTC	0.96	2.39±0.22	384±60	5653±2×10^3	Yagi *et al.*, 2009
24a	Haiti	2010-01-12/21:53:10 UTC	0.99	2.71±0.25	122±16	6330±1×10^3	Gorum *et al.*, 2013
24b	Haiti	2010-01-12/21:53:10 UTC	0*	2.26±0.07	39±8	2674±5×10^2	Harp *et al.*, 2016
25	Sierra Cucapah (Mexico)	2010-04-04/22:40:42 UTC	0.13	2.61±0.12	496±113	1457±1×10^2	Barlow *et al.*, 2015
26	Yushu (China)	2010-04-13/23:49:38 UTC	0.01*	2.26±0.33	106±15	581±6×10^2	Xu *et al.*, 2013
27	Eastern Honshu (Japan)	2011-03-11/05:46:24 UTC	0.87	2.90±0.29	97±18	1916±6×10^2	Wartman *et al.*, 2013
28a	Lushan (China)	2013-04-20/00:02:47 UTC	0.67	2.63±0.20	496±97	5726±1×10^3	Li *et al.*, 2013
28b	Lushan (China)	2013-04-20/00:02:47 UTC	0.94	2.93±0.21		5359±1×10^3	Xu *et al.*, 2015
29	Minxian-Zhangxian (China)	2013-07-21/23:45:56 UTC	0.78	2.27±0.11	106±15	228±6×10^2	Xu *et al.*, 2014a
30	Ludian (China)	2014-08-03/08:30:13 UTC	0.99	2.46±0.18	761±139	9234±2×10^3	Tian *et al.*, 2015
31a	Gorkha (Nepal)	2015-05-12/07:05:19 UTC	0.68	2.40±0.08	1397±193	5210±1×10^3	Zhang *et al.*, 2016
31b	Gorkha (Nepal)	2015-05-12/07:05:19 UTC	0.95	2.04±0.09	135±17	8461±1×10^3	Tanyas *et al.*, 2018
31c	Gorkha (Nepal)	2015-05-12/07:05:19 UTC	0*	2.49±0.11	211±38	1344±1×10^3	Roback *et al.*, 2017
32a	Kumamoto (Japan)	2016-04-15/16:25:06 UTC	0.79	2.44±0.29	377±114	6249±2×10^3	DSPR-KU, 2016
32b	Kumamoto (Japan)	2016-04-15/16:25:06 UTC	0.56	2.02±0.14	192±25	2362±1×10^3	NIED, 2016

*Inventory does not meet the criteria for a power-law based on the Kolmogorov–Smirnov statistic.

(2004) also are shown for comparison. Results show that power-law scaling at medium to large landslide areas exists for 39 inventories having *P*-value larger than 0.1 (Tanyaş *et al.*, 2018) (Table I), whereas all of them diverge from power-law scaling for smaller areas (Figure 2). The FADs for medium to large landslides of many of the inventories match the shape, though not necessarily the slope of the modeled rollover of Malamud *et al.* (2004). Most of the FADs plot below the theoretical curves, which Malamud *et al.* (2004) interprets as an indicator of incompleteness. Some inconsistencies are difficult to explain. For example, the FADs of some inventories extend beyond the empirical curves at small landslide areas (Figure 2(g)–(h)). In these inventories, the rollover point is not located where predicted by the empirical curves. In fact, for a significant number of EQIL inventories, the form and position of the rollover do not follow the modeled empirical distribution curves. Furthermore, we observe FADs without an obvious rollover for some inventories such as the Guatemala (Harp *et al.*, 1981), Coalinga (Harp and Keefer, 1990), Loma Prieta (McCrink, 2001), Kiholo Bay (Harp *et al.*, 2014) and Lushan (Xu *et al.*, 2015) inventories (Figure 2(h)). This implies that existing rollover explanations need to be reevaluated.

Rollover and cutoff sizes

We plot the rollover points of all EQIL inventories in the same graph for comparison (Figure 3(a)). This plot shows that the
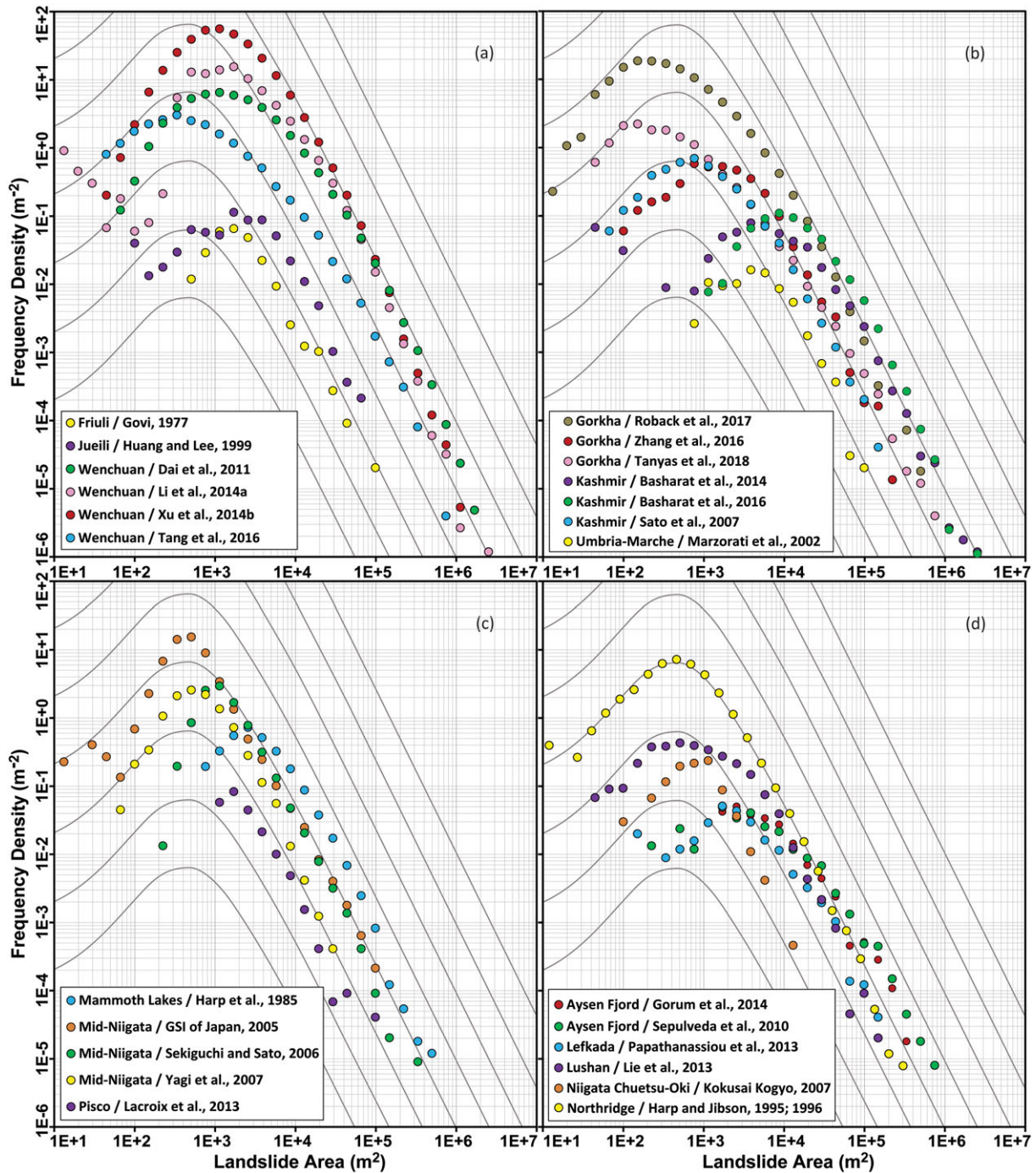
Figure 2. FADs of the landslide inventories used in this study, grouped by FAD shape similarity from (a) to (h), overlain on the empirical curves of Malamud *et al.* (2004) which are shown in black. [Colour figure can be viewed at wileyonlinelibrary.com]

2010 Haiti inventory of Harp *et al.* (2016), which also is well documented and one of the most complete inventories in this EQIL inventory database (Tanyaş *et al.*, 2018), gives the smallest rollover size (~40 m²) with the highest frequency density value (y-axis in a FAD graph). At the other end of the spectrum, the 2002 Denali inventory of Gorum *et al.* (2014) has the largest rollover size (~16 000 m²). Gorum *et al.* (2014) noted that many small landslides might not have been mapped in this inventory because of low-resolution satellite imagery. However, the meaning of this large rollover size should not entirely be associated with the poor resolution of the interpreted imagery; many other studies use imagery of similarly low resolution (Figure 3(b)). Also, it could reflect real differences in the distribution. For example, Jibson *et al.* (2004) stated that compared

with comparable or lower magnitudes earthquakes, the Denali earthquake had significantly lower concentrations of rock-falls and rock slides and proposed that this was because the earthquake was deficient in high-frequency energy and attendant high-amplitude accelerations. This argument requires a comprehensive analysis considering the dominant frequencies of earthquakes that is beyond the scope of this study.

We compare the rollover sizes with the cutoff values (R^2=0.333 and RMSE=0.486) (Figure 4(a)). Although the results show no one-to-one relation between rollover and cutoff values, the increasing cutoff values correlate generally with increasing rollover values. Also, we plot both the rollover and cutoff values in relation to imagery resolution (Figure 4(b) and 4(c)). The lack of systematic patterns shows that high-resolution
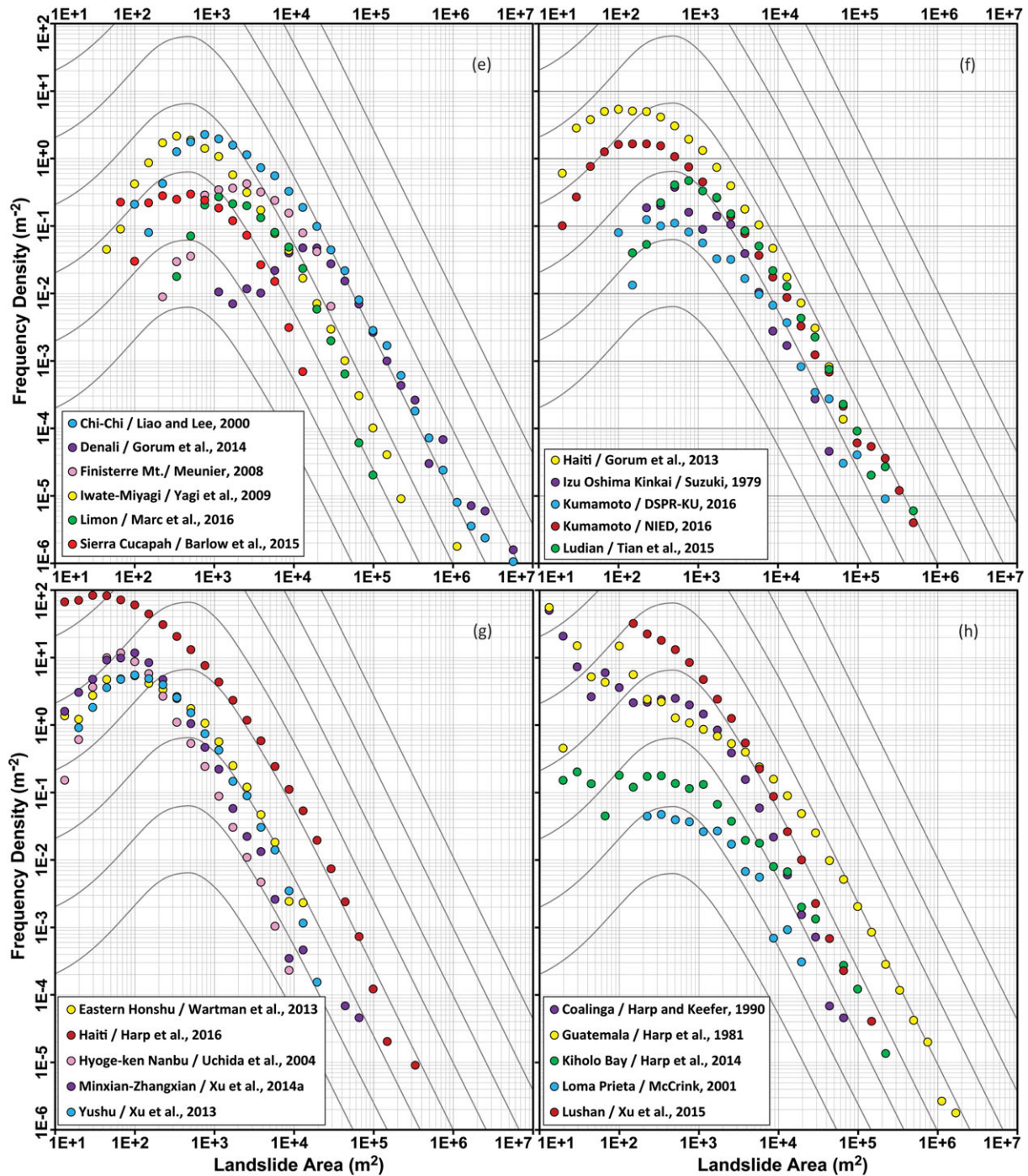
Figure 2. (continued)

imagery is not required to have a small rollover or cutoff value and vice versa. However, the results do reveal that only the smallest rollovers occur with the highest resolution imagery. This implies that spatial resolution partly controls the rollover point but that other factors also contribute to the divergence from a power-law.

Proposed hypotheses

Here, we analyze the different proposed rollover hypotheses using examples from the data presented above.

Hypothesis 1 argues that the divergence/rollover is an artifact based on limitations in mapping small landslides. But most event inventories that claim to be complete, which means they

include virtually all landslides triggered by the corresponding event down to a well-defined size, also have a rollover (Guzzetti *et al.*, 2002; Malamud *et al.*, 2004). If the divergence were purely a mapping artifact, a very large number of small landslides should be observable following earthquakes, but field investigations and published comprehensive landslide inventories show this not to be the case (Malamud *et al.*, 2004).

To demonstrate this contrast between the theoretical expectation and the field data, we analyze the FAD from the Northridge inventory (Harp and Jibson, 1995, 1996), which used high-altitude analog aerial photography and thus might have inadequate resolution to detect very small landslides. Figure 5 shows the Northridge data diverging from the power-law fit around landslide areas of 9000 m². However, Harp and Jibson (1995, 1996) estimated that they missed no more
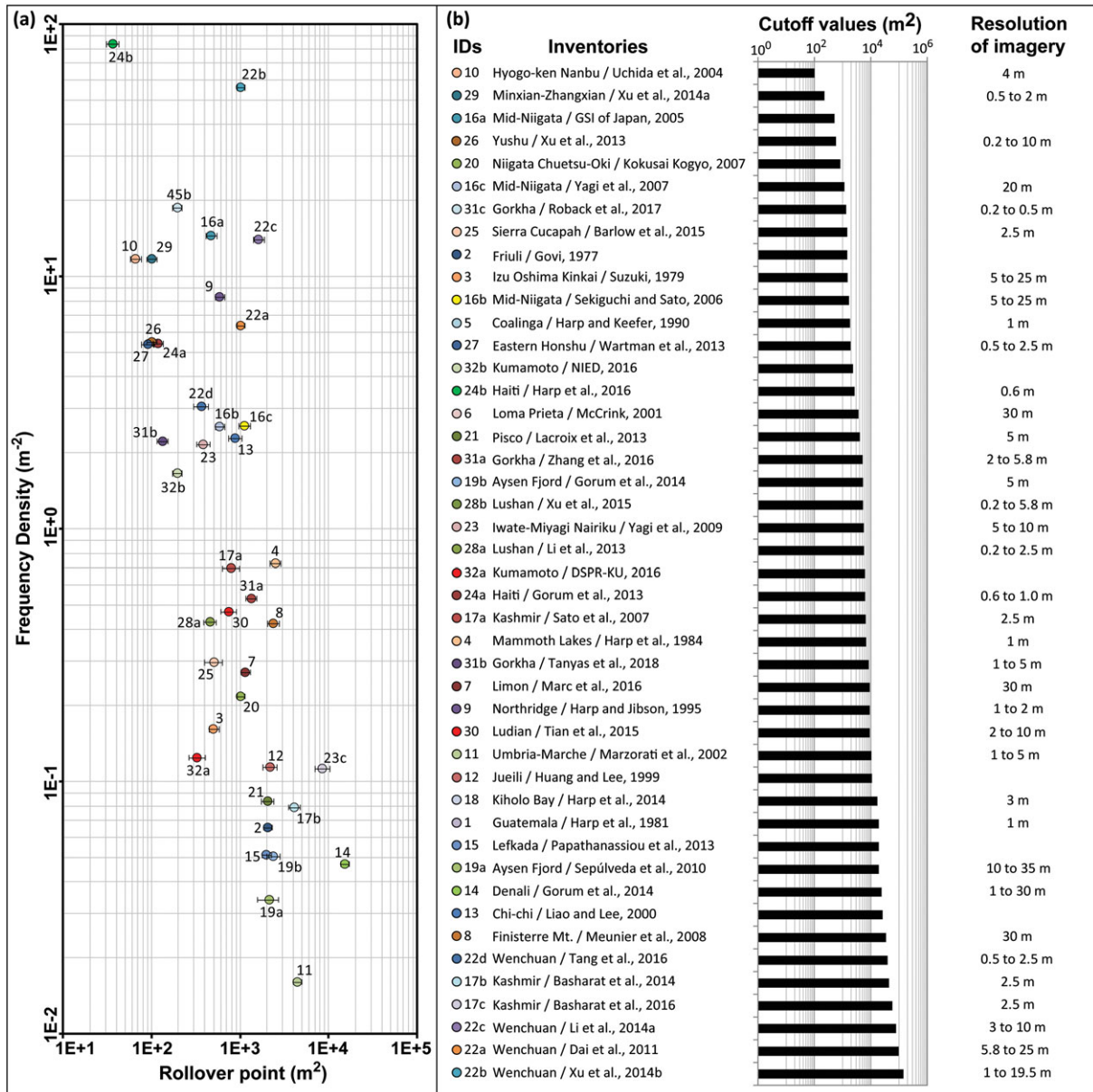
Figure 3. Graphs showing the (a) distribution of rollover points, and (b) the inventories with the scale/resolution of imageries used sorted in descending order according to their cutoff values. [Colour figure can be viewed at wileyonlinelibrary.com]

than about 20% of landslides greater than 5 m in maximum dimension and no more than 50% of those smaller than 5 m. They also estimated that they mapped more than 90% of the area covered by landslides, which suggests that most of the landslides larger than 5 m across (≈25 m^2) were mapped in the Northridge inventory.

This resolution estimate differs significantly from the cutoff value. If, in fact, Harp and Jibson (1995, 1996) could not map the small landslides as completely as they thought because of inadequate image resolution, then the FAD for a theoretically complete version of the inventory should follow a power-law also for small landslides. To test this argument, we construct a power-law curve for the Northridge inventory (Figure 5). Based on this theoretical distribution, we calculate the number of landslides for each bin from 25 m^2 to the cutoff point (≈9000 m^2). For each bin, we also estimate the number of landslides that theoretically should exist and calculate the difference between these values and the number of landslides in the same bins for the actual inventory. The results indicate that more than 8 million more landslides would have been triggered than were mapped in the existing Northridge inventory of Harp and Jibson (1995, 1996). Even if landslides smaller than

1000 m^2 are eliminated, more than 20 000 landslides would be missing from the inventory, which is double the entire number of landslides in the inventory. Also, we estimate the number of theoretically missing landslides for other inventories (Figure S1, Supplementary material) using the same method. We tentatively select the lower landslide bin of 25 m^2 for these estimations. Results show that the number of theoretically missing landslides ranges between 3×10^3 and 4×10^{10}, which indicates a dramatic, implausible contradiction between the hypothesis and the data. Thus, it appears that mapping resolution alone is inadequate to explain the power-law divergence.

Hypothesis 2 argues that a change in the underlying failure process from small, shallow failures located in soil and regolith to large, deep bedrock slides causes rollover due to the transition from shear resistance controlled by cohesion to friction. However, we do not know the underground conditions in each landslide-affected area, which would be necessary to evaluate this argument. On the other hand, Larsen *et al.* (2010) assume that landslides that are smaller than about 100 000 m^2 are generally a combination of both bedrock and soil failures; larger landslides are assumed to be entirely in bedrock. But this does not provide a consistent definition for shallow and deep
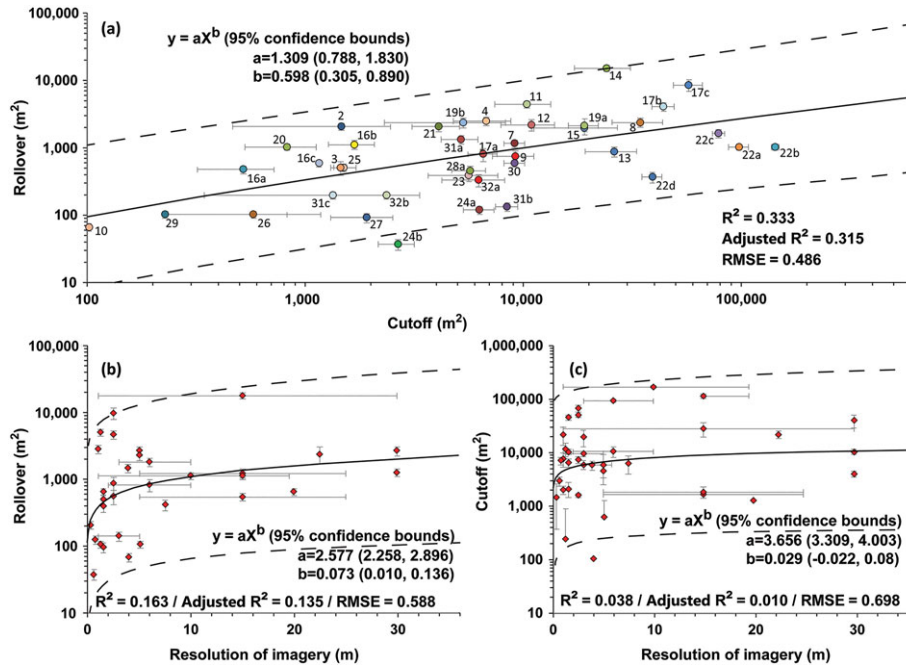
Figure 4. Graphs showing the relation between (a) the cutoff and the rollover points, and (b) the rollover and (c) the cutoff values in relation to the resolution of imagery used during the mapping of landslides. 95% confidence intervals for the true responses are indicated by dashed lines. [Colour figure can be viewed at wileyonlinelibrary.com]
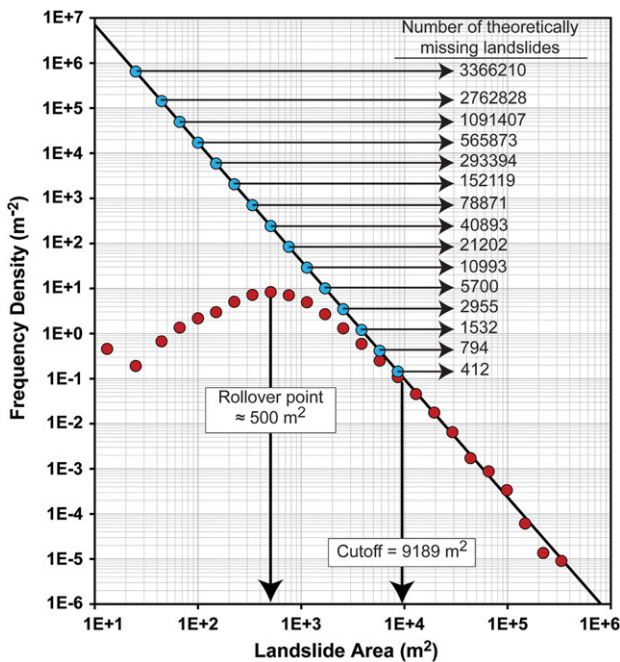

Figure 5. Non-cumulative FAD and its power-law fit for the landslide inventory of the 1994 Northridge earthquake (Harp and Jibson, 1995, 1996). The differences between the number of landslides based on the inventory and the power-law fit are indicated. Power-law exponents (–2.62) and cutoff values (9189 m^2) were estimated using the methodology presented by Clauset *et al.* (2009). [Colour figure can be viewed at wileyonlinelibrary.com]

landslides because Larsen *et al.* (2010) also show that, for example, small landslides (~10 m^2) can involve bedrock at a depth ranging from 0.1 to 10 m. Therefore, landslide size is not a reliable measure to estimate the underlying material.

Figure 3 shows variety in cutoff values from around 10^2 to 10^5 m^2. For example, in the 2008 Wenchuan inventory (Xu *et al.*, 2014b) the observed cutoff value is around 144 000 m^2 (Table I), which corresponds roughly to a landslide width of about 400 m. *Hypothesis 2* would suggest landslides 144 000 m^2 as the cutoff for small, shallow landslides located within the top soil layer of the hillslope lacking cohesion compared with deeper bedrock. Published studies from Wenchuan, however indicate that rock slides and rock avalanches are moderately common in the Wenchuan inventory, whereas soil slides are much less numerous (Gorum *et al.*, 2011). Xu *et al.* (2014b) state that only 2% of the area affected by landslides is located within unconsolidated deposits. However, landslides smaller than 144 000 m^2 constitute about 50% of total area affected by landslides. This implies that there were many bedrock slides smaller than the observed cutoff value (<144 000 m^2). Figure 3 also shows 15 inventories having cutoff values larger than 10^4 m^2. As discussed above, classifying such landslides as small soil failures is problematic.

An example from the other end of the spectrum is the Hyogo-ken Nanbu inventory (Uchida *et al.*, 2004), where the cutoff point is 102 m^2 (Table I). Fukuoka *et al.* (1997) report that many shallow debris slides and soil slides were triggered by this earthquake. Similarly, Gerolymos (2008) states that most landslides originated within unsaturated soil. That is why, in this case, the question is why a divergence from the power-law up to the size of 100 m^2 is not observed. Therefore, although *Hypothesis 2* does probably account for some of the small-landslide divergence, this explanation appears unable to consistently explain the power-law divergence for each inventory (Table I).

Hypothesis 3 argues that the distribution of soil moisture associated with river networks controls the geometry of landslides. This argument might not apply to earthquake-induced landslides, however, where slides tend to be triggered preferentially in upslope areas rather than along stream networks and are strongly influenced by topographic amplification (Guzzetti *et al.*, 2002). Shallow landslides in upslope areas, which account for a large proportion of all earthquake-triggered landslides (Keefer, 1984) are unlikely to be affected by soil-moisture conditions related to river drainages far downslope. Also, the landslide-affected area of some inventories (e.g., Harp and Jibson, 1995, 1996) was arid, yet extensive seismically induced landsliding still occurred.

To more thoroughly examine *Hypothesis 3*, we analyze the EQIL inventory database. In each inventory, we calculate the drainage density of the study area, which is the sum of the channel lengths per unit area (Carlston, 1963). To do that, we first derive the river channel network using the r.stream.extract module (Peter, 1994) of GRASS GIS (Neteler and Mitasova, 2013) and then calculate drainage density per square kilometer. We use the Shuttle Radar Topography Mission (SRTM) ~30-m-resolution digital elevation model (NASA Jet Propulsion Laboratory (JPL), 2013) in the analyses. We also use GRASS GIS (Neteler and Mitasova, 2013) r.geomorphon code developed by Jasiewicz and Stepinski (2013) to identify 10 landform classes (flat, summit, ridge, shoulder, spur, slope, hollow, footslope, valley and depression). This algorithm calculates landforms and associated geometry using pattern recognition. The algorithm self-adapts to identify the most suitable spatial scale at each location and check the visibility of the neighborhood to assign one of the terrestrial forms. We mask flat regions and exclude them for the estimation of drainage densities because the river channel network algorithm gives errors in flat regions. We compare the drainage densities to both rollover and cutoff values (Figure S2) and see no relation between either of them. These findings are not sufficient to reject the possible contribution of this approach to the divergence from power-law, but they imply that other process (es) contribute to the divergence.

Hypothesis 4 associates the lack of small landslides with physiographic limitations (slope length) and considers runout zones as an integral part of landslides. However, as described above, landslide deposits (runouts) bias the FAD of landslides, and an ideal inventory would omit runout and only use the source area to define the size of the landslide. *Hypothesis 4* suggests that most regions have more areas where large landslides can occur than where small landslides can occur. According to this hypothesis, the upper parts of slopes should be dominated by medium and large landslides, whereas the small landslides should be observed at the lower parts of slopes or on shorter slopes. To test this hypothesis, we analyze the 2015 Gorkha (Roback *et al.*, 2017) inventory where the authors mapped almost all of the source areas separately. We check the size distribution of landslides for lower, middle and upper parts of slopes. To do so, we use the various landforms that we derive above for the entire landslide-affected area of the Gorkha earthquake. We then categorize the obtained landform classes based on their relative position along a slope. We group the summit, ridge, and shoulder landform classes as observable landforms occurring in the upper slope; we associate slope, spur, and hollow with middle slopes. The other landforms, including flat, footslope, and valley, are associated with lower slopes. We calculate zonal statistics for all landslide source polygons and identify the dominant landform category for each landslide. We use the landform class with the most area inside the landslide polygon to identify the dominant landform category. Finally, we check the landslide size distributions for each of the slope segments (Figure 6). Results show quite similar size distributions in different slope segments. Landslides of all sizes occur in each part of the slope. Therefore, the suggested physiographic argument does not seem to explain why the FAD diverges from the negative power-law-distribution.

Hypothesis 5 associates the divergence from a power-law with a lack of temporal resolution. However, there is only one case study supporting this argument by monitoring rock-falls on a slope (Williams *et al.*, 2018). Validity of this hypothesis for other types of landslide-events has not been checked so far. Therefore, further analyses in other cases and developing a conceptual understanding of this hypothesis are required.

In addition to the above-mentioned hypotheses aiming to explain the divergence from a power-law, there are some factors
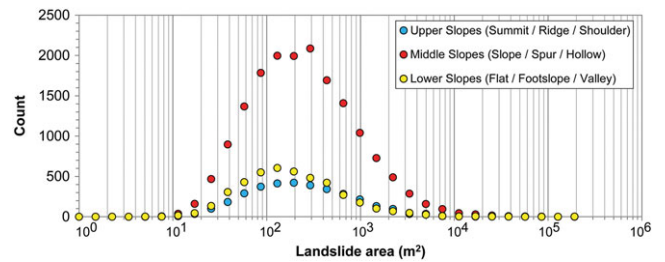

Figure 6. Landslide size distributions for different segments of a hillslope differentiated based on various landform groups. [Colour figure can be viewed at wileyonlinelibrary.com]

controlling FADs of landslides. These factors are analyzed in the following section.

Amalgamation due to lack of spatial resolution and mapping preferences

Landslide inventories are created for different purposes and thus both the spatial resolution of examined images and the time invested in making an inventory vary. Figure 7 shows an example of amalgamation for the 2015 Gorkha earthquake. The number and boundaries of landslides in this area cannot be determined in a strictly objective way (Figure 7(a)). Different mapping preferences produce different landslide sizes and numbers (Figure 7(b)–(d)). In Figure 7(b)–(d), we map this area using progressively more detailed approaches, and the result is landslide counts that vary by almost a factor of 3. But all three inventories would be considered valid. Figure 7(b) does not differentiate coalescing landslides; the resulting inventory (Set 1) contains 88 landslides. Figure 7(c) differentiates some of the coalesced landslides that show clear color differences; the resulting landslide Set 2 contains 184 mapped landslides. Figure 7(d) differentiates landslides as much as possible based on both color and textural differences; the result is 253 mapped landslides (Set 3). This shows that when higher resolution images are available, more detailed mapping is possible, and even more landslides can be differentiated.

The same area was mapped by different authors; the resulting landslide numbers are 19 (Kargel *et al.*, 2016), 32 (Zhang *et al.*, 2016), 40 (Tanyaş *et al.*, 2018), 42 (Gnyawali and Adhikari, 2017), and 151 (Roback *et al.*, 2017).

This example shows that the number of landslides mapped in the same area by different people differed by almost an order of magnitude, and our application of different mapping approaches yielded a difference of a factor of 3. Different mapping methods do not significantly affect the total landslide area, but they have an important effect on the landslide FAD. Figure 8 shows the FADs of the landslide sets created in this example. From Set 1 to Set 3 the sizes of the biggest landslides decrease, and the rollover points shift toward smaller landslide sizes because the number of small landslides increases. Similarly, because we divide the amalgamated landslides into smaller ones from Set 1 to Set 3, the ratio of small to large landslides increases, and therefore the corresponding power-law exponents also increase.

Subjectivity of mapping procedure

To demonstrate the effect of subjectivity of mapping procedures on the resulting FAD, we examine earthquakes for which multiple inventories were produced and compare their FADs (Figure S3). To provide comparable FADs from each earthquake, we trim the inventories to the same extent as the
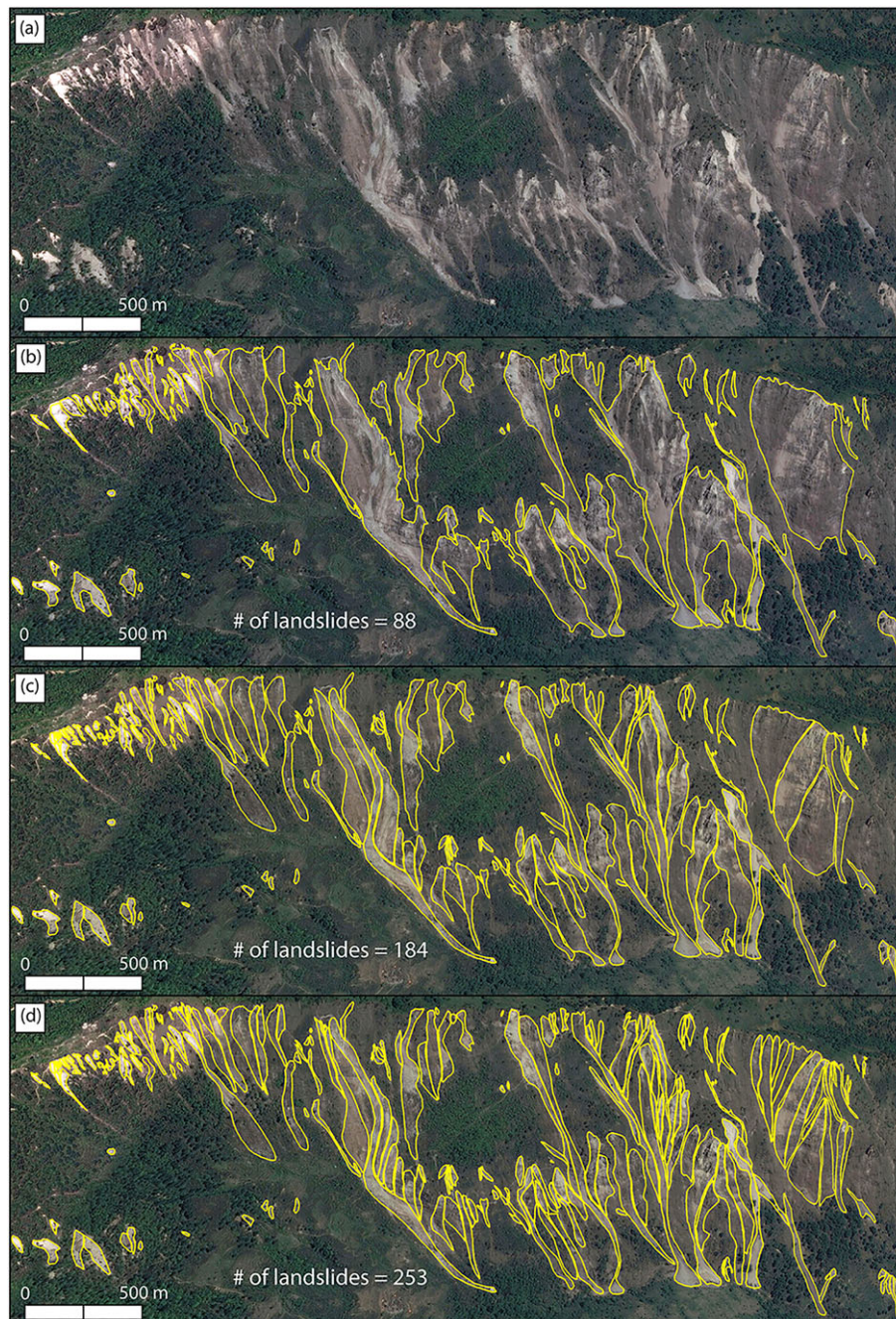
Figure 7. An example of an EQIL site near the town of Gumda (28.199°lat, 84.853°lon) from the 2015 Gorkha earthquake: (a) source photograph showing landslides, (b) landslide delineation using maximum amalgamation, (c) landslide delineation using moderate amalgamation, and (d) detailed landslide delineation separating landslides to the maximum extent possible (minimal amalgamation). [Colour figure can be viewed at wileyonlinelibrary.com]

smallest one. As result, we examine landslides from different inventories mapped for the same areal extent. We plot the FADs using the landslides mapped for those areal extents and compare the resulting total number of landslides, total landslide areas (sums of polygon areas), power-law exponents, and rollover sizes (Figure S3). Figure 9 shows two examples of the explained comparison of the inventories provided for the 2010 Haiti and 2005 Kashmir earthquakes; Figure 10 shows the differences between total number of landslides, total landslide areas, power-law exponents, and rollover sizes for all cases. For the same areal extent, the 2010 Haiti inventory of Harp *et al.* (2016) includes 16 379 more landslides than the inventory provided by Gorum *et al.* (2013). This is the largest difference observed in terms of the total number of landslides (Figure 10). For the same areal extent, the difference in the total mapped landslide area in these inventories is 16.9 km^2. We

also calculate the total landslide area of completely overlapping polygons of different inventories. The total landslide area mapped by Gorum *et al.* (2013) is 5.9 km^2, but 20% of those landslides do not overlap with the polygons delineated by Harp *et al.* (2016). Thus, in total, Harp *et al.* (2016) mapped about 18 km^2 of coseismic landslides that Gorum *et al.* (2013) did not. This means that in this case amalgamation is not the main reason for the significant difference between these two inventories. The inventories were produced using similar visual image-interpretation approaches using detailed images (with a spatial resolution of 0.6–1 m), although Harp *et al.* (2016) did the mapping more carefully over a much longer time period than did Gorum *et al.* (2013).

The difference between the FADs of the Haiti inventories (Figure 9(c)) implies that a similar number of medium and large landslides (>10^3 km^2) were mapped in both studies, but Harp
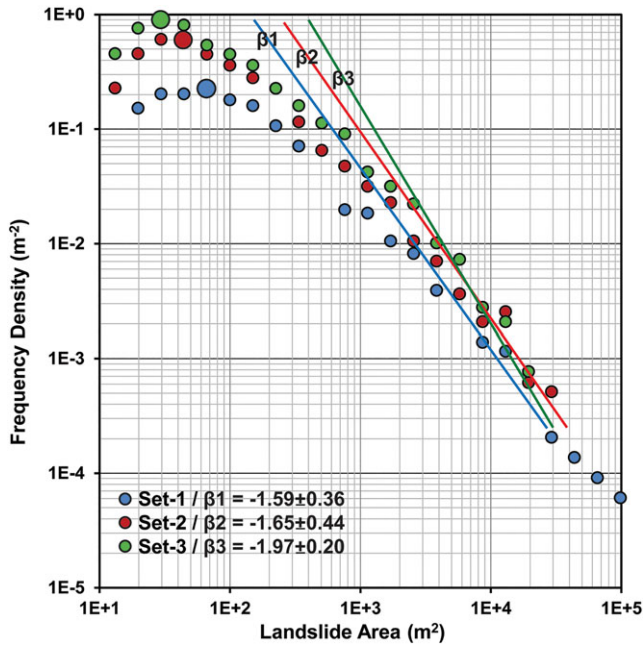
Figure 8. FADs and their corresponding power-law fit of different landslide sets presented in Figure 7. Larger dots indicate rollover points. [Colour figure can be viewed at wileyonlinelibrary.com]

et al. (2016) mapped a large number of small landslides ($<10^3$ km^2) not mapped by Gorum *et al.* (2013). The FAD of the Harp *et al.* (2016) inventory has a smaller rollover point (~30 m^2) and larger power-law exponent (β=2.89) than the Gorum *et al.* (2013) inventory (~100 m^2 and β=2.09). These results are consistent with Figure 8, but in this case the differences cannot be attributed to amalgamation of coalescing or adjacent landslides but the subjectivity of the mapping procedures.

We also analyzed three inventories from the 2005 Kashmir earthquake (Figure 9(b) and 9(d)). The 2005 Kashmir inventories yield the largest difference in total landslide area mapped for the same areal extent (Figure 9(d)). The total landslide area mapped by Basharat *et al.* (2016) is 33.6 km^2 (420%) larger than the area mapped by Sato *et al.* (2007). The total landslide area mapped by Sato *et al.* (2007) is 8.0 km^2, and only 45% of this landslide area overlaps with the polygons delineated by Basharat *et al.* (2016). However, Sato *et al.* (2007) mapped 127 more landslides than did Basharat *et al.* (2016). These two Kashmir inventories used a similar mapping method and the same satellite imagery (SPOT 5). These two inventories are quite different although they are from the same event, have the same areal extent, and used the same mapping method. Their FADs also are quite different, and the rollover point is much smaller in the Sato *et al.* (2007) inventory (~760 m^2) compared with the Basharat *et al.* (2016) inventory (~8650 m^2). In
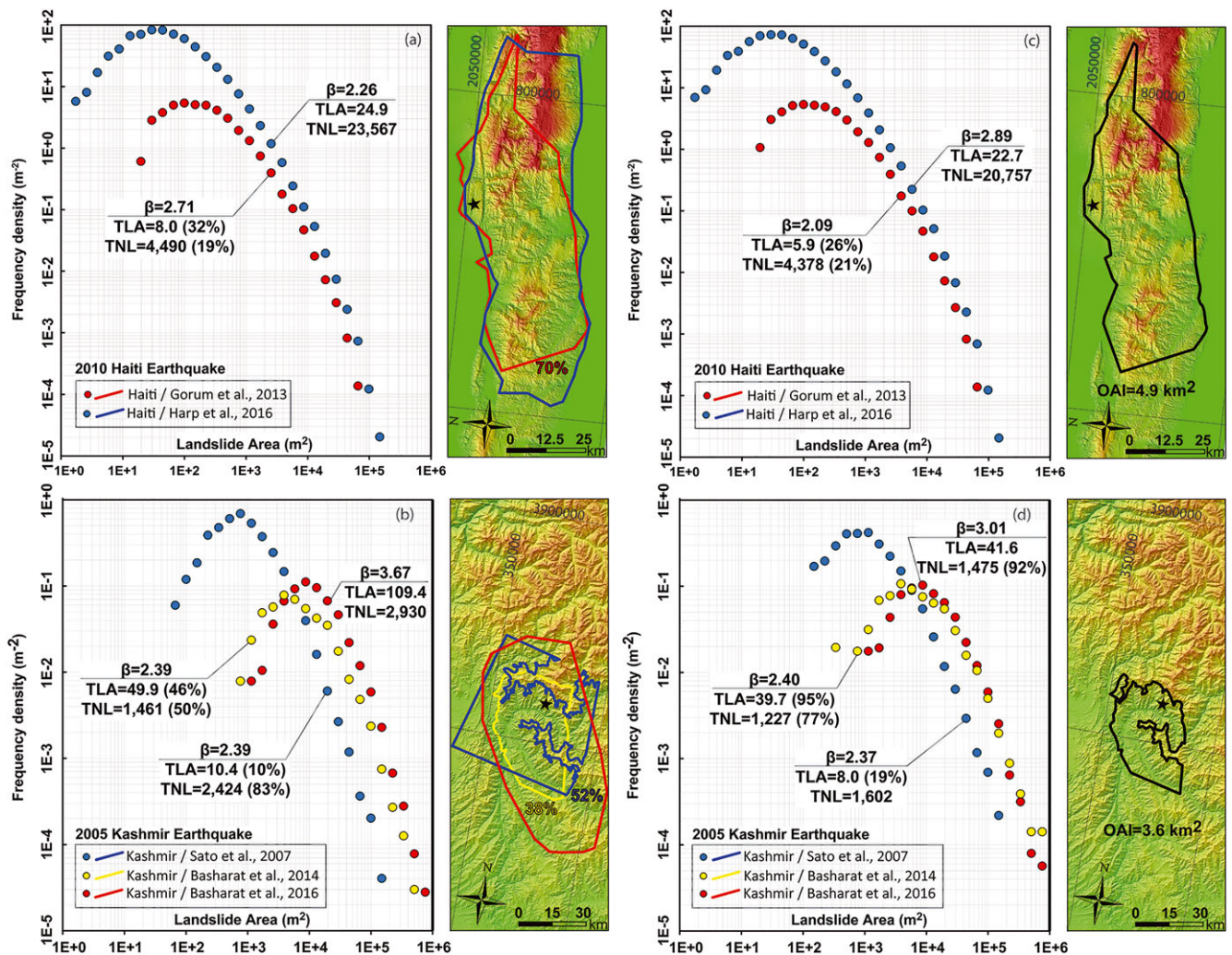

Figure 9. FADs of inventories produced for (a) and (b) the same earthquakes with the extent of the corresponding inventories' mapped areas, and (c) and (d) the trimmed versions of them for the common areas. TLA: Total landslide area (km^2), TNL: Total number of landslides, OAI: Overlapping areas of inventories. [Colour figure can be viewed at wileyonlinelibrary.com]
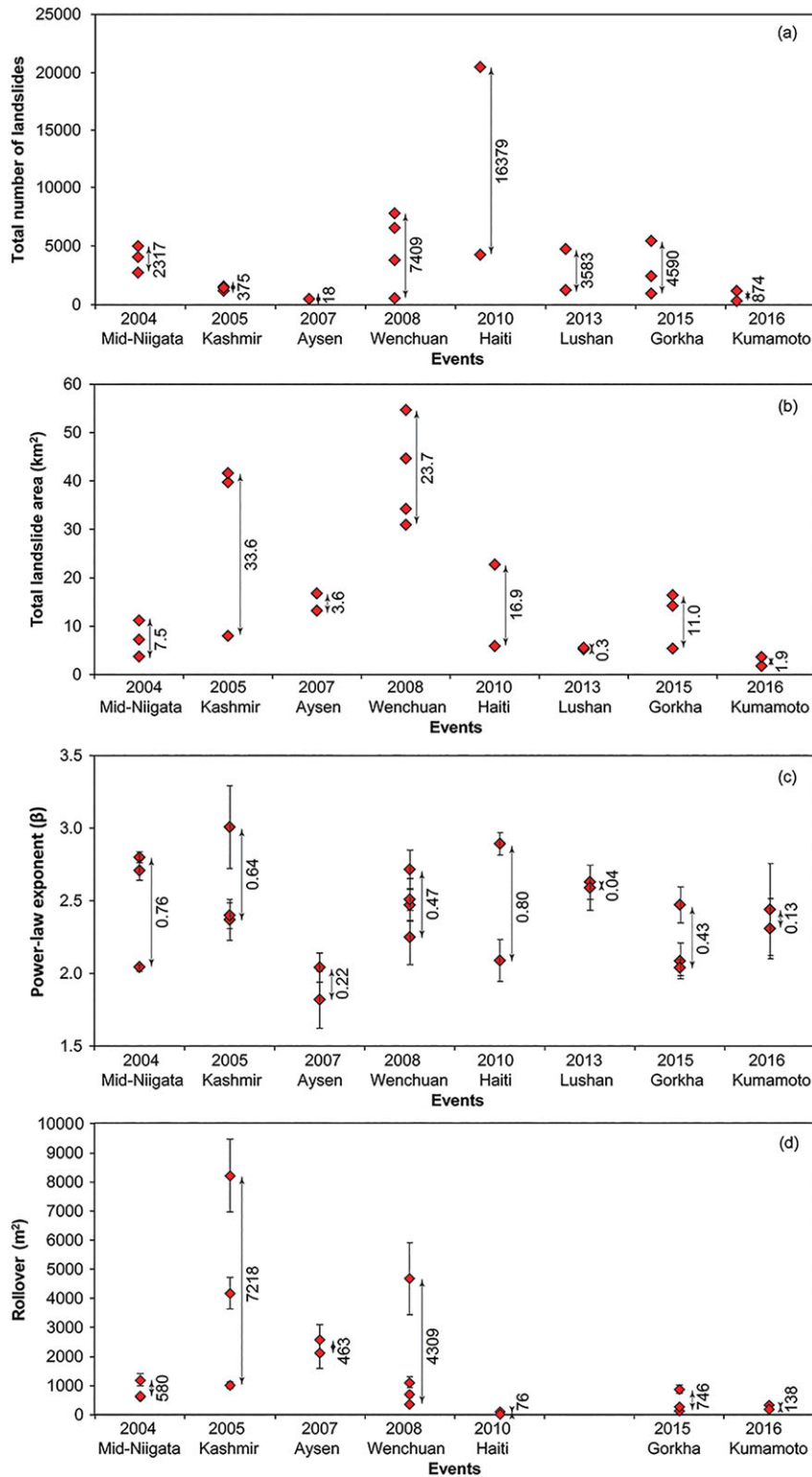
Figure 10. Variability in (a) total number of landslides, (b) total landslide area (c) β, and (d) rollover sizes for the events having multiple inventories. To plot this figure, we trimmed the inventories to the same extent as the smallest one. [Colour figure can be viewed at wileyonlinelibrary.com]

contrast, however, the Basharat *et al.* (2016) inventory has a higher power-law exponent (β=3.01) than the Sato *et al.* (2007) inventory (β=2.37).

Figure 9 shows that mapping preferences could cause a large difference in FADs of landslides and related factors such as β. The largest difference between power-law exponents in the examined cases is the Haiti example with 0.80 (Figure 10). Considering the power-law exponent of the Haiti inventory of Gorum *et al.* (2013) (β=2.09±0.80), the difference is 38% of the calculated value. This shows that the uncertainty in β values caused by mapping preferences can be as much as 38%. Korup

et al. (2012) state that minute numerical errors in model parameters of FADs can cause uncertainty greater than a factor of 2 in erosion or mobilization rates. Thus, we can expect a large uncertainty, for example, in denudation rate (Hovius *et al.*, 1997) because of this variance in β.

Several studies have explored the relation between variations in β with regional differences in structural geology, morphology, hydrology and climate (Sugai *et al.*, 1995; Densmore *et al.*, 1998; Dussauge-Peisser *et al.*, 2002; Chen, 2009; Li *et al.*, 2011; Bennett *et al.*, 2012; Hergarten, 2012). However, the analyses presented above reveal that the uncertainties are

likely too high to discriminate physical regional differences. This is because regardless of these factors and despite the similarities in terms of overall mapping methodology and images used, differences in mapping skills, mapping criteria, thresholds of minimum landslides that are mapped, and the time dedicated to mapping might result in very different inventories. As a result, FADs of landslides and related factors such as β are exposed to an intrinsic noise caused by the subjectivity of the mapping procedure. Regrettably, quantifying the quality of the inventories directly from FADs is impossible without re-mapping the landslides from the original imagery from which the inventories were made. Thus, further standardization of landslide mapping procedures and proper metadata of landslide inventories that explain the mapping procedure and time investments are the only ways to minimize this noise and potentially, one day, be able to resolve the signal of regional differences.

Effect of distinguishing between landslide sources and deposits on FAD shape

Some inventories distinguish landslide sources from deposits, at least for larger landslides. The FADs and rollover points in such inventories differ somewhat from those of inventories where landslides are mapped as a single polygon without differentiating erosion and accumulation areas. In the 2004 Mid-Niigata (GSI of Japan, 2005) inventory, large and small landslides are defined separately, and for the large landslides the sources and deposits were mapped separately. For the 2004 Mid-Niigata (GSI of Japan, 2005) and the 2015 Gorkha inventories (Roback *et al.*, 2017), we divide the landslides into two sets. In Set 1, the sources and deposits of landslides are considered together; in Set 2 the deposits of large landslides are ignored, and we only consider the source areas (Figure 11).

The exclusion of landslide deposits in Set-2 decreases the size of individual landslides and shifts the position of the entire FAD toward smaller sizes. The rollover points also shift from 3850 m^2 to 1700 m^2 (Figure 11(a)) and from 210 m^2 to 30 m^2 (Figure 11(b)) in the Mid-Niigata and the Gorkha inventories, respectively.

Figure 11 shows significant differences between FADs from source-only inventories and those constructed using entire landslide polygons. However, a rollover in the FAD is present even when landslide deposits are excluded.
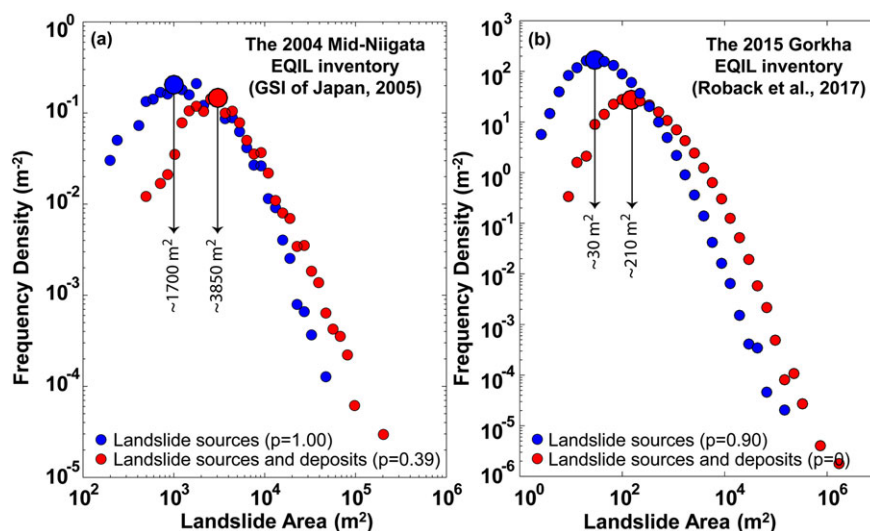
We also check numerically the validity of a power-law fit for both versions of the Mid-Niigata and the Gorkha inventories. Results show that in both cases size distributions of landslide source areas have significantly larger *P*-values (better fits) than size distributions considering sources and deposits of landslides together (Figure 11). In the Mid-Niigata case, both versions of the inventory have *P*-values larger than 0.1, whereas the *P*-value of Set 1 for the 2015 Gorkha earthquake is 0. This shows that the Roback *et al.* (2017) Gorkha inventory that includes deposits does not fit a power-law. However, for the same inventory, the exclusion of landslide deposits yields a good power-law fit with a *P*-value of 1. These findings show that differentiation of source and deposit areas strongly affects the resultant FAD.

Discussion

Several hypotheses have been proposed for the causes of the deviation from a power-law relation for smaller landslides. Our findings show that each hypothesis helps us to grasp a part of the phenomenon but no single existing explanation accounts for the deviation and rollover in all cases, and different factors contribute to explain the causes of the rollover in different cases. Especially, lack of spatial image resolution and details of the underlying failure process as proposed in previously published studies clearly contribute to the divergence from the power-law. Additionally, lack of temporal resolution also is a considerable factor because identifying each individual landslide event that actually occurred is impeded by lack of temporal resolution. We approach this issue within the context of successive slope failure, as described below.

A proposed explanation for the divergence from the power-law: Successive slope failure

A single mapped landslide polygon can be the result of successive episodes of movement and enlargement. Frattini and Crosta (2013) referred to this issue and stated that even for accurate inventories of single events, many smaller landslides can be undetectable because of reworking during the event by larger coalescent landslides. For example, earthquake shaking can cause part of a slope to collapse, which creates a scarp and a runout zone. The scarp itself can be unstable and further fail and expand afterward; this produces an additional

Figure 11. FADs for different subsets of (a) the 2004 Mid-Niigata (GSI of Japan, 2005), and (b) the Gorkha (Roback *et al.*, 2017) EQIL inventories. Larger dots indicate rollover points. [Colour figure can be viewed at wileyonlinelibrary.com]

landslide above the first one, but this subsequent landslide will be mapped as part of the original failure. This process can occur in succession during a later part of the shaking of the mainshock or as a result of aftershocks, subsequent rainfall, or progressive failure owing to weakened soil material and changes in the slope stress field. Thus, what we observe as a single landslide polygon is a snapshot of the geometry of an accumulation of successive sliding events at the time the imagery was collected; the slope will continue to evolve indefinitely as it adapts to the new conditions (Figure S4). Therefore, the inverse-cascade model (see Supplementary material), which is the qualitative explanation provided for the fractal distribution of landslides (Malamud and Turcotte, 2006), should be valid for the formation of mapped individual landslides. As we described above, the inverse-cascade model suggests that slope instability begins at a location and spreads to surrounding metastable areas. The landslide population formed as a result of this process has a fractal size distribution. As the inverse-cascade model is applied to slopes shaken by earthquakes, we call this sliding process successive slope failure.

Successive slope failure encompasses processes such as progressive and retrogressive failures, which are specific mechanisms that can contribute to successive slope failure (Figure S5). Progressive slope failure is a common mode of failure that occurs in cohesive materials such as clays (Bjerrum, 1967). In progressive slope failure, after the initiation of the first landslide, the scarp is in a metastable condition, and a second slide begins to mobilize from the scarp area sometime after the initial slide (Bjerrum, 1967). This can continue to cascade upslope through the progressive propagation of a shear surface along which shear strength is reduced from peak to residual values. This occurs because shear strength is not constant along a potential failure surface in cohesive materials; the strength changes from peak to residual (Bjerrum, 1967). Thus, spatial and temporal strength heterogeneities are the cause of progressive failures. Successive slope failure applies more generally than progressive failure because successive slope failure occurs in different types of soil and rock. For example, Terzaghi (1962) described rock masses generally as media having discontinuous joints differing in persistence. Intact rock bridges occur between these discontinuous joints. Failures begin with the failure of an individual rock bridge and keep occurring successively as the shear strength of each individual bridge is exceeded.

Eberhardt *et al.* (2004) modeled the rock-mass strength degradation in natural rock slopes based on the conceptual framework of Terzaghi (1962). They show that stresses ahead of the shear plane increase and subsequent intact rock bridges fail in a consecutive manner until the surface of failure extends to the point where kinematic release becomes possible.

Successive slope failure also can occur as a result of retrogressive failure, which refers to a specific failure geometry wherein a failure zone migrates upslope (Cruden and Varnes, 1996). However, successive slope failure is much more general than retrogressive failure; it can involve destabilization of slopes laterally, upslope, downslope, or by several mechanisms and geometries. It is simply the process of an initial slope failure destabilizing surrounding areas.

Samia *et al.* (2017) investigated the same concept from another point of view. They examined the landslide path dependency using a multi-temporal landslide inventory from Italy. They concluded that earlier landslides affect the susceptibility of future landslides; larger and rounder landslides are more likely to cause follow-up failures.

Successive slope failure might not apply to landslides in massive rocks where failure commonly is controlled by discontinuities such as faults, fractures, shear zones, bedding planes and joints (Hoek and Brown, 1997). Such discontinuities isolate the landslide mass from the rest of the slope. Therefore, for rock-falls, having a frequency-size distribution without rollover is understandable in some cases (Malamud *et al.*, 2004). Even in this situation, however, landslide margins are likely to produce smaller, continuing failures as the disturbed topography seeks equilibrium. For example, Williams *et al.* (2018) showed a rollover in frequency-size distribution of rock-falls if mapping is conducted using a low temporal resolution.

The interpretation of the proposed explanation

The successive-slope-failure hypothesis, which extends the argument raised for rock-falls in *Hypothesis 5* (Barlow *et al.*, 2012; Williams *et al.*, 2018) provides a conceptual model to explain the power-law divergence. Figure 12 presents this hypothesis schematically in terms of FAD; landslide numbers observed at different size bins are shown. Figure 12(a) shows a theoretical FAD assuming that all EQIL triggered during the event are detected and that landslide FADs across all size
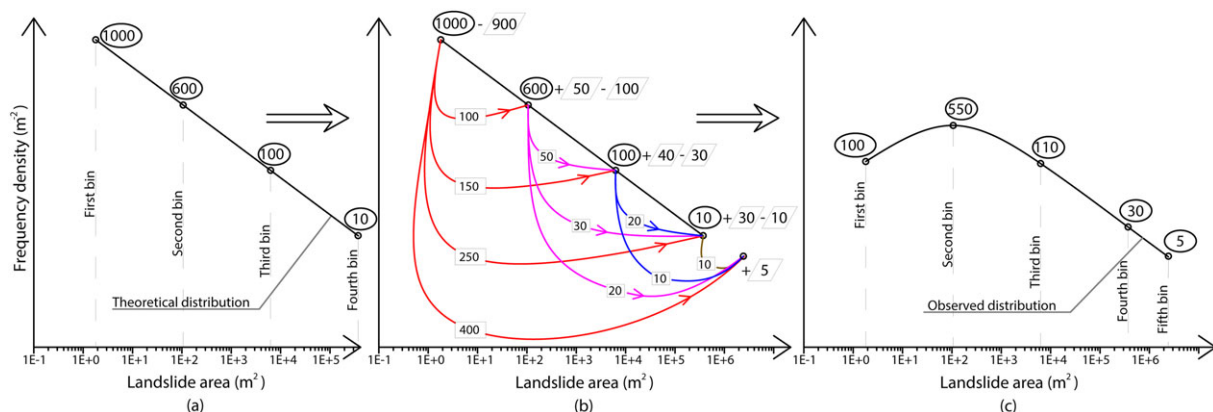

Figure 12. Schematic drawing showing the number of landslides of different sizes in different theoretical situations. (a) Theoretical FAD of landslides if all individual landslides were mapped perfectly. (b) Smaller landslides are amalgamated or mapped inside larger ones. For example, 900 small landslides in the first bin are merged into larger ones; 100 landslides into the second bin; 150 into the third bin; etc. (c) The resulting observed FAD with rollover. The numbers shown in ovals and parallelograms indicate the initial/final and transferred number of landslides, respectively. The numbers of landslides transferred from smaller bins to larger ones are not equal to each other because multiple small landslides merged together and formed fewer larger landslides. The given landslide numbers are partially arbitrary; both the numbers of landslides in each bin and the numbers of landslides transferred from smaller bins to larger ones have a decreasing trend from small to larger landslide sizes. [Colour figure can be viewed at wileyonlinelibrary.com]

ranges follow a pure power-law behavior. However, in practice, larger landslides are mapped because many smaller ones that occur at the initiation of sliding are incorporated into larger ones or are mapped together into amalgamated polygons (Figure 12(b)). Additionally, some of the smaller landslides are superimposed by larger ones. Therefore, some landslides could not be mapped into their correct size bins, and they are transferred into a larger landslide bin. This causes identification of more large landslides because the smaller slides merge into larger ones. This also causes identification of fewer total landslides, particularly in the smaller size range, than theoretically expected based on the power-law distribution assumption; this, in turn, causes the divergence from the power-law distribution (Figure 12(c)). Without conducting a continuous monitoring, capturing the effect of this misclassification on small landslide bins is not possible. Thus, the misclassification of landslide size bins might or might not cause a distinctive decrease in small landslide bins. If it is distinctive, a rollover and positive power-law decay for smaller landslide sizes emerges (Figure 12(c)). This is observed in most of the inventories presented in this study (Figure 2). If the effect of unmapped small landslides is less distinct, landslide FADs still diverge from a power-law distribution but do not show a rollover point. Figure 2(h) shows such an unusual trend in the FADs for the Coalinga (Harp and Keefer, 1990), Guatemala (Harp et al., 1981), and Lushan (Xu et al., 2015) inventories. This likely reflects the complicated interplays between mapping methodology, landslide amalgamation, and the successive-landslide-formation process on the final FAD.

This explanation implies that neither divergence from the negative power-law distribution of medium and large landslides nor a positive power-law distribution for landslides smaller than the rollover point are attributable to the incompleteness of an inventory; both of these characteristics can occur in complete landslide inventories. In our proposed explanation, some of the small landslides that could not be mapped in the correct size bins are included in the larger bins; therefore, an inventory with a rollover can be relatively complete in terms of total mobilized landslide area.

Our proposed explanation suggests that neither the rollover nor cutoff points indicate the exact lower landslide size at which the inventory can be assumed to be complete (Van Den Eeckhaut et al., 2007; Parker et al., 2015). Because we generally do not know the minimum landslide size where mapping is nearly complete, the rollover point can be used as an upper-bound estimate of that value.

The proposed explanation also suggests that mapping many medium and large landslides should inevitability cause misclassification of a relatively large number of small landslides, and this leads to a shift in both rollover and cutoff values towards larger sizes (see Figure 12). To test this argument, we arbitrarily select three landslide sizes of $1000\,m^2$, $2500\,m^2$, and $5000\,m^2$ as the thresholds between small and medium landslides, and we correlate both the rollover and cutoff points with the percentages of landslides having areas greater than $1000\,m^2$, $2500\,m^2$, and $5000\,m^2$ (Figure S6). The results confirm our argument and show that in an inventory that includes a relatively large number of large landslides both the rollover and cutoff values shift toward larger sizes compared with inventories having relatively few large landslides. This finding provides evidence to support our hypothesis about the cause of FAD rollover.

Additionally, as presented above, the findings of Barlow et al. (2012) and Williams et al. (2018) derived for rock-falls also support our conceptual model to explain the power-law divergence. However, this conceptual model still needs to be proven by high temporal resolution slope monitoring.

Conclusions

This study examines the factors controlling the FADs of landslide inventories and provides an alternative explanation for the deviation from power-law scaling observed in the FADs by analyzing 45 EQIL inventories. All existing rollover explanations described above provide a partial understanding of why landslide FADs do not follow the power-law theory for small landslides. Although not all explanations contribute to each case, each inventory probably involves some combination of the proposed explanations.

We propose an additional explanation: successive slope failure, in which smaller slides sequentially destabilize surrounding slopes and merge to form larger slides that are detectable after the earthquake.

Studies by Barlow et al. (2012) and Williams et al. (2018) demonstrate the importance of temporal resolution on rock-fall FADs and provide observational support for our hypothesis. We use this argument and present a theoretical background with all findings obtained from 45 EQIL inventories showing that the actual number of coalesced landslides within each landslide polygon is unknown because we lack the necessary time resolution of observations used for mapping. This means that low time resolution, a mapping artifact, is one of the reasons for the divergence from the power-law. Therefore, the divergence from a power-law does not necessarily imply incompleteness of an inventory.

Additionally, we show that mapping methodology, amalgamation of coalescing landslides due to the quality and resolution of the imagery, the level of expertise of mappers, and undifferentiated landslide source and deposit areas causes intrinsic noise in landslide FADs. These factors contribute in various combinations to determine the FAD shape, which is defined by the power-law exponent, cutoff point, and rollover. That is why the shape of a FAD, and thus β, can vary significantly because of the complicated interplay between the given factors. The uncertainty in β values caused by these factors can be as much as 38% (e.g. β=2.09±0.80 in Haiti inventory of Gorum et al. (2013)). A 38% uncertainty can cause substantial errors in prediction of erosion rates (Korup et al., 2012) and landslide hazard assesments (Guzzetti et al., 2005) because of the resulting divergence in both landslide-event magnitude and probabilities of landslide size.

Based on these findings, our analyses lead to four main conclusions. First, the rollover point generally is at a larger landslide area than the lower limit of completely mapped landslide size of the inventory. Second, various mapping techniques can yield different total numbers of landslides, and thus the number of landslides is a subjective measure. Third, the FAD-based completeness evaluation of Malamud et al. (2004) needs to be revised. Finally, inventories that depict landslide source areas separately from depositional areas yield more physically meaningful FADs for EQIL inventories.

The highlighted uncertainty in FADs of landslides implies that the power-law derived from a low-quality inventory does not describe landslides very well. This shows the need for a standard mapping methodology to be able to obtain more consistent and quantitative information about landslides from FAD comparisons. Working with compatible inventories can help in modeling FADs of EQIL inventories more accurately. Such a FAD model also can help better quantify landslide event inventories and provide a reasonable basis to evaluate the completeness of inventories. Reliable FADs of EQIL also can help improve our knowledge regarding landscape evolution processes.

References

Barlow J, Barisin I, Rosser N, Petley D, Densmore A, Wright T. 2015. Seismically-induced mass movements and volumetric fluxes resulting from the 2010 Mw=7.2 earthquake in the Sierra Cucapah, Mexico. *Geomorphology* **230**: 138–145. https://doi.org/10.1016/j.geomorph.2014.11.012.

Barlow J, Lim M, Rosser N, Petley D, Brain M, Norman E, Geer M. 2012. Modeling cliff erosion using negative power-law scaling of rockfalls. *Geomorphology* **139-140**: 416–424. https://doi.org/10.1016/j.geomorph.2011.11.006.

Basharat M, Ali A, Jadoon IA, Rohn J. 2016. Using PCA in evaluating event-controlling attributes of landsliding in the 2005 Kashmir earthquake region, NW Himalayas, Pakistan. *Natural Hazards* **81**: 1999–2017. https://doi.org/10.1007/s11069-016-2172-9.

Basharat M, Rohn J, Baig MS, Khan MR. 2014. Spatial distribution analysis of mass movements triggered by the 2005 Kashmir earthquake in the Northeast Himalayas of Pakistan. *Geomorphology* **206**: 203–214. https://doi.org/10.1016/j.geomorph.2013.09.025.

Bennett G, Molnar P, Eisenbeiss H, McArdell B. 2012. Erosional power in the Swiss Alps: characterization of slope failure in the Illgraben. *Earth Surface Processes and Landforms* **37**: 1627–1640. https://doi.org/10.1002/esp.3263.

Bjerrum L. 1967. Progressive failure in slopes of overconsolidated plastic clay and clay shales. *Journal of the Soil Mechanics and Foundations Division of the American Society of Civil Engineers* **93**: 1–49.

Brardinoni F, Church M. 2004. Representing the landslide magnitude–frequency relation: Capilano River basin, British Columbia. *Earth Surface Processes and Landforms* **29**: 115–124.

Carlston CW. 1963. Drainage density and streamflow: U.S. Geological Survey Professional Paper 422-C, 8 p. https://pubs.er.usgs.gov/publication/pp422C.

Chen C-Y. 2009. Sedimentary impacts from landslides in the Tachia River Basin, Taiwan. *Geomorphology* **105**: 355–365.

Clauset A, Shalizi CR, Newman ME. 2009. Power-law distributions in empirical data. *SIAM review* **51**: 661–703. https://doi.org/10.1137/070710111.

Cruden DM, Varnes DJ. 1996. Landslide types and process. In *Landslides: Investigation and Mitigation*, Turner AK, Schuster RJ (eds), Special report 247. Transportation Research Board, National Research Council, National Academy Press: Washington DC; 36–75.

Dai F, Xu C, Yao X, Xu L, Tu X, Gong Q. 2011. Spatial distribution of landslides triggered by the 2008 Ms 8.0 Wenchuan earthquake, China. *Journal of Asian Earth Sciences* **40**: 883–895. https://doi.org/10.1016/j.jseaes.2010.04.010.

Davison FC, Scholz CH. 1985. Frequency-moment distribution of earthquakes in the Aleutian Arc: a test of the characteristic earthquake model. *Bulletin of the Seismological Society of America* **75**: 1349–1361.

Densmore AL, Ellis MA, Anderson RS. 1998. Landsliding and the evolution of normal-fault-bounded mountains. *Journal of Geophysical Research: Solid Earth* **103**: 15203–15219.

DSPR-KU. 2016. Slope movement condition by 2016 Kumaoto earthquake in Minami-Aso village (as of 19:00 JST on 18 Apr 2016), edited, Disaster Prevention Research Institute, Kyoto University, http://www.slope.dpri.kyoto-u.ac.jp/disaster_reports/2016KumamotoEq/2016KumamotoEq2.html (in Japanese).

Dussauge-Peisser C, Helmstetter A, Grasso J-R, Hantz D, Desvarreux P, Jeannin M, Giraud A. 2002. Probabilistic approach to rock fall hazard assessment: Potential of historical data analysis. *Natural Hazards and Earth System Science* **2**: 15–26.

Eberhardt E, Stead D, Coggan J. 2004. Numerical analysis of initiation and progressive failure in natural rock slopes—the 1991 Randa rockslide. *International Journal of Rock Mechanics and Mining Sciences* **41**: 69–87.

Frattini P, Crosta GB. 2013. The role of material properties and landscape morphology on landslide size distributions. *Earth and Planetary Science Letters* **361**: 310–319. https://doi.org/10.1016/j.epsl.2012.10.029.

Fukuoka H, Sassa K, Scarascia-Mugnozza G. 1997. Distribution of Landslides Triggered by the 1995 Hyogo-ken Nanbu Earthquake and Long Runout Mechanism of the Takarazuka Golf Course Landslide. *Journal of Physics of the Earth* **45**: 83–90.

GSI of Japan (Geospatial Information Authority of Japan). 2005.1:25,000 Damage Map of the Mid Niigata Prefecture Earthquake in 2004: 3sheets.

Gerolymos N. 2008. Analysis of Two case histories of violent landslides triggered by earthquakes. In *International Conference on Case Histories in Geotechnical Engineering*, Vol. **7**. http://scholarsmine.mst.edu/icchge/6icchge/session13/7.

Gnyawali KR, Adhikari BR. 2017. Spatial Relations of Earthquake Induced Landslides Triggered by 2015 Gorkha Earthquake Mw = 7.8. In *Advancing Culture of Living with Landslides: Volume 4 Diversity of Landslide Forms*, Mikoš M, Casagli N, Yin Y, Sassa K (eds). Springer International Publishing: Cham; 85–93.

Gorum T, Fan X, van Westen CJ, Huang RQ, Xu Q, Tang C, Wang G. 2011. Distribution pattern of earthquake-induced landslides triggered by the 12 May 2008 Wenchuan earthquake. *Geomorphology* **133**: 152–167. https://doi.org/10.1016/j.geomorph.2010.12.030.

Gorum T, Korup O, van Westen CJ, van der Meijde M, Xu C, van der Meer FD. 2014. Why so few? Landslides triggered by the 2002 Denali earthquake, Alaska. *Quaternary Science Reviews* **95**: 80–94. https://doi.org/10.1016/j.quascirev.2014.04.032.

Gorum T, van Westen CJ, Korup O, van der Meijde M, Fan X, van der Meer FD. 2013. Complex rupture mechanism and topography control symmetry of mass-wasting pattern, 2010 Haiti earthquake. *Geomorphology* **184**: 127–138. https://doi.org/10.1016/j.geomorph.2012.11.027.

Govi M. 1977. Photo-interpretation and mapping of the landslides triggered by the Friuli earthquake (1976). *Bulletin of the International Association of Engineering Geology-Bulletin de l'Association Internationale de Géologie de l'Ingénieur* **15**: 67–72. https://doi.org/10.1007/BF02592650.

Guthrie R, Evans S. 2004. Magnitude and frequency of landslides triggered by a storm event, Loughborough Inlet, British Columbia. *Natural Hazards and Earth System Science* **4**: 475–483. https://doi.org/10.5194/nhess-4-475-2004.

Guthrie RH, Deadman PJ, Cabrera AR, Evans SG. 2008. Exploring the magnitude–frequency distribution: A cellular automata model for landslides. *Landslides* **5**: 151–159. https://doi.org/10.1007/s10346-007-0104-1.

Guzzetti F, Malamud BD, Turcotte DL, Reichenbach P. 2002. Power-law correlations of landslide areas in central Italy. *Earth and Planetary Science Letters* **195**: 169–183. https://doi.org/10.1016/S0012-821X(01)00589-1.

Guzzetti F, Reichenbach P, Cardinali M, Galli M, Ardizzone F. 2005. Probabilistic landslide hazard assessment at the basin scale. *Geomorphology* **72**: 272–299. https://doi.org/10.1016/j.geomorph.2005.06.002.

Harp EL, Hartzell SH, Jibson RW, Ramirez-Guzman L, Schmitt RG. 2014. Relation of Landslides Triggered by the Kiholo Bay Earthquake to Modeled Ground Motion. *Bulletin of the Seismological Society of America* **104**: 2529–2540. https://doi.org/10.1785/0120140047.

Harp EL, Jibson RW. 1995. Inventory of landslides triggered by the 1994 Northridge, California earthquake: U.S. Geological Survey Open-File Report. 95–213.

Harp EL, Jibson RW. 1996. Landslides triggered by the 1994 Northridge, California earthquake. *Bulletin of the Seismological Society of America* **86**: 319–332.

Harp EL, Jibson RW, Schmitt RG. 2016. Map of landslides triggered by the January 12, 2010, Haiti earthquake: U.S. Geological Survey

Scientific Investigations Map 3353, 15 p., 1 sheet, scale 1:150,000. https://pubs.er.usgs.gov/publication/sim3353.

Harp EL, Keefer DK. 1990. Landslides triggered by the earthquake. In *The Coalinga, California, Earthquake of May 2, 1983*, Rymer MJ, Ellsworth WL (eds), Vol. **1487**, US Geological Survey Professional Paper; 335–347.

Harp EL, Tanaka K, Sarmiento J, Keefer DK. 1984. Landslides from the May 25–27, 1980, Mammoth Lakes, California, earthquake sequence. U.S. Geological Survey Miscellaneous Investigations Series Map. https://pubs.er.usgs.gov/publication/i1612.

Harp EL, Wilson RC, Wieczorek GF. 1981. Landslides from the February 4, 1976, Guatemala earthquake, U.S. Geological Survey Professional Paper 1204-A, 35 p, 2 plates. https://pubs.er.usgs.gov/publication/pp1204A.: Washington.

Hergarten S. 2003. Landslides, sandpiles, and self-organized criticality. *Natural Hazards and Earth System Science* **3**: 505–514.

Hergarten S. 2012. Topography-based modeling of large rockfalls and application to hazard assessment. *Geophysical Research Letters* **39** L13402. DOI: https://doi.org/10.1029/2012GL052090.

Hoek E, Brown ET. 1997. Practical estimates of rock mass strength. *International Journal of Rock Mechanics and Mining Sciences* **34**: 1165–1186.

Hovius N, Stark CP, Allen PA. 1997. Sediment flux from a mountain belt derived by landslide mapping. *Geology* **25**: 231–234. https://doi.org/10.1130/0091-7613(1997)025<0231:SFFAMB>2.3.

Huang TF, Lee CT. 1999. Landslides triggered by the Jueili earthquake. In *Proceedings of the*. Annual Meeting of the Geological Society of China: Taipei; 1999.

Hungr O, Evans S, Hazzard J. 1999. Magnitude and frequency of rock falls and rock slides along the main transportation corridors of southwestern British Columbia. *Canadian Geotechnical Journal* **36**: 224–238.

Jasiewicz J, Stepinski TF. 2013. Geomorphons — a pattern recognition approach to classification and mapping of landforms. *Geomorphology* **182**: 147–156. https://doi.org/10.1016/j.geomorph.2012.11.005.

Jibson RW, Harp EL, Schulz W, Keefer DK. 2004. Landslides triggered by the 2002 Denali fault, Alaska, earthquake and the inferred nature of the strong shaking. *Earthquake spectra* **20**: 669–691. https://doi.org/10.1193/1.1778173.

Kargel JS, Leonard GJ, Shugar DH, Haritashya UK, Bevington A, Fielding EJ, Fujita K, Geertsema M, Miles ES, Steiner J, Anderson E, Bajracharya S, Bawden GW, Breashears DF, Byers A, Collins B, Dhital MR, Donnellan A, Evans TL, Geai ML, Glasscoe MT, Green D, Gurung DR, Heijenk R, Hilborn A, Hudnut K, Huyck C, Immerzeel WW, Jiang Liming, Jibson R, Kääb A, Khanal NR, Kirschbaum D, Kraaijenbrink PDA, Lamsal D, Liu Shiyin, Mingyang Lv, McKinney D, Nahirnick NK, Nan Zhuotong, Ojha S, Olsenholler J, Painter TH, Pleasants M, KC P, Yuan Q, Raup BH, Regmi D, Rounce DR, Sakai A, Shangguan Donghui, Shea JM, Shrestha AB, Shukla A, Stumm D, van der Kooij M, Voss K, Wang Xin, Weihs B, Wolfe D, Wu Lizong, Yao Xiaojun, Yoder MR, Young N. 2016. Geomorphic and geologic controls of geohazards induced by Nepal's 2015 Gorkha earthquake. *Science* **351**: 6269. https://doi.org/10.1126/science.aac8353

Katz O, Aharonov E. 2006. Landslides in vibrating sand box: What controls types of slope failure and frequency magnitude relations? *Earth and Planetary Science Letters* **247**: 280–294.

Keefer DK. 1984. Landslides caused by earthquakes. *Geological Society of America Bulletin* **95**: 406–421. https://doi.org/10.1130/0016-7606(1984)95<406:LCBE>2.0.CO;2.

Kogyo K. 2007. *Aerial photo interpretation of earthquake damage from the 2007 Niigata Chuetsu–oki Earthquake*. Kokusai Kogyo Co., Ltd: Japan.

Korup O, Görüm T, Hayakawa Y. 2012. Without power? Landslide inventories in the face of climate change. *Earth Surface Processes and Landforms* **37**: 92–99.

Lacroix P, Zavala B, Berthier E, Audin L. 2013. Supervised method of landslide inventory using panchromatic SPOT5 images and application to the earthquake-triggered landslides of Pisco (Peru, 2007, Mw8. 0). *Remote Sensing* **5**: 2590–2616. https://doi.org/10.3390/rs5062590.

Larsen IJ, Montgomery DR, Korup O. 2010. Landslide erosion controlled by hillslope material. *Nature Geoscience* **3**: 247–251. https://doi.org/10.1038/ngeo776.

Li C, Ma T, Zhu X, Li W. 2011. The power–law relationship between landslide occurrence and rainfall level. *Geomorphology* **130**: 221–229.

Li G, West AJ, Densmore AL, Jin Z, Parker RN, Hilton RG. 2014. Seismic mountain building: Landslides associated with the 2008 Wenchuan earthquake in the context of a generalized model for earthquake volume balance. *Geochemistry, Geophysics, Geosystems* **15**: 833–844. https://doi.org/10.1002/2013GC005067.

Li W-l, Huang R-q, Xu Q, Tang C. 2013. Rapid susceptibility mapping of co-seismic landslides triggered by the 2013 Lushan Earthquake using the regression model developed for the 2008 Wenchuan Earthquake. *Journal of Mountain Science* **10**: 699–715. https://doi.org/10.1007/s11629-013-2786-2.

Liao H-W, Lee C-T. 2000. Landslides triggered by the Chi-Chi earthquake. In Proceedings of the 21st Asian conference on remote sensing; 383–388.

Malamud BD, Turcotte DL. 2006. *An inverse cascade explanation for the power-law frequency–area statistics of earthquakes, landslides and wildfires*, Vol. **261**. Geological Society, London, Special Publications; 1–9.

Malamud BD, Turcotte DL, Guzzetti F, Reichenbach P. 2004. Landslide inventories and their statistical properties. *Earth Surface Processes and Landforms* **29**: 687–711. https://doi.org/10.1002/esp.1064.

Marc O, Hovius N. 2015. Amalgamation in landslide maps: effects and automatic detection. *Natural Hazards and Earth System Science* **15**: 723–733. https://doi.org/10.5194/nhess-15-723-2015.

Marc O, Hovius N, Meunier P, Gorum T, Uchida T. 2016. A seismologically consistent expression for the total area and volume of earthquake-triggered landsliding. *Journal of Geophysical Research: Earth Surface* **121**: 640–663. https://doi.org/10.1002/2015JF00373.

Marzorati S, Luzi L, De Amicis M. 2002. Rock falls induced by earthquakes: a statistical approach. *Soil Dynamics and Earthquake Engineering* **22**: 565–577. https://doi.org/10.1016/S0267-7261(02)00036-2.

McCrink PT. 2001. Regional Earthquake-Induced Landslide Mapping Using Newmark Displacement Criteria, Santa Cruz County, California. In *Engineering Geology Practice in Northern California*, Ferriz H, Anderson (eds), Vol. **210**, California Geological Survey Bulletin. Association of Engineering Geologists Special Publication 12; 77–93.

Meunier P, Hovius N, Haines JA. 2008. Topographic site effects and the location of earthquake induced landslides. *Earth and Planetary Science Letters* **275**: 221–232. https://doi.org/10.1016/j.epsl.2008.07.020.

NASA Jet Propulsion Laboratory (JPL). 2013. NASA Shuttle Radar Topography Mission United States 1 arc second. NASA EOSDIS Land Processes DAAC, USGS Earth Resources Observation and Science (EROS) Center, Sioux Falls, South Dakota (https://lpdaac.usgs.gov), accessed January 1, 2015.

Neteler M, Mitasova H. 2013. *Open source GIS: A GRASS GIS approach*. Springer Science & Business Media.

NIED (National Research Institute for Earth Science and Disaster Resilience). 2016. Distribution map of mass movement by the 2016 Kumamoto earthquake, edited by National Research Institute for Earth Science and Disaster of Japan, http://www.bosai.go.jp/mizu/dosha.html. (in Japanese).

Papathanassiou G, Valkaniotis S, Ganas A, Pavlides S. 2013. GIS-based statistical analysis of the spatial distribution of earthquake-induced landslides in the island of Lefkada, Ionian Islands, Greece. *Landslides* **10**: 771–783. https://doi.org/10.1007/s10346-012-0357-1.

Parker R, Hancox G, Petley D, Massey C, Densmore A, Rosser N. 2015. Spatial distributions of earthquake-induced landslides and hillslope preconditioning in the northwest South Island, New Zealand. *Earth Surface Dynamics* **3**: 501. https://doi.org/10.5194/esurf-3-501-2015.

Parker RN, Densmore AL, Rosser NJ, de Michele M, Li Y, Huang R, Whadcoat S, Petley DN. 2011. Mass wasting triggered by the 2008 Wenchuan earthquake is greater than orogenic growth. *Nature Geoscience* **4**: 449–452. https://doi.org/10.1038/ngeo1154.

Pelletier JD, Malamud BD, Blodgett T, Turcotte DL. 1997. Scale-invariance of soil moisture variability and its implications for the frequency-size distribution of landslides. *Engineering Geology* **48**: 255–268. https://doi.org/10.1016/S0013-7952(97)00041-0.

Peter H. 1994. Multiple flow direction algorithms for runoff modelling in grid based elevation models: An empirical evaluation. *Hydrological Processes* **8**: 327–334. https://doi.org/10.1002/hyp.3360080405.

Roback K, Clark MK, West AJ, Zekkos D, Li G, Gallen SF, Champlain D, Godt JW. 2017. Map data of landslides triggered by the 25 April 2015 Mw 7.8 Gorkha, Nepal earthquake: U.S. Geological Survey data release. DOI: https://doi.org/10.5066/F7DZ06F9

Samia J, Temme A, Bregt A, Wallinga J, Guzzetti F, Ardizzone F, Rossi M. 2017. Do landslides follow landslides? Insights in path dependency from a multi-temporal landslide inventory. *Landslides* **14**: 547–558. https://doi.org/10.1007/s10346-016-0739-x.

Sato HP, Hasegawa H, Fujiwara S, Tobita M, Koarai M, Une H, Iwahashi J. 2007. Interpretation of landslide distribution triggered by the 2005 Northern Pakistan earthquake using SPOT 5 imagery. *Landslides* **4**: 113–122. https://doi.org/10.1007/s10346-006-0069-5.

Schmitt RG, Tanyas H, Nowicki Jessee MA, Zhu J, Biegel KM, Allstadt KE, Jibson RW, Thompson EM, van Westen CJ, Sato HP, Wald DJ, Godt JW, Gorum T, Xu C, Rathje EM, Knudsen KL. 2017. An open repository of earthquake-triggered ground-failure inventories. In Data Series: Reston, VA; 26.

Sekiguchi T, Sato HP. 2006. Feature and distribution of landslides induced by the Mid Niigata Prefecture Earthquake in 2004, Japan. *Journal of the Japan Landslide Society* **43**: 142–154.

Sepúlveda S, Serey A, Lara M, Pavez A, Rebolledo S. 2010. Landslides induced by the April 2007 Aysén Fjord earthquake, Chilean Patagonia. *Landslides* **7**: 483–492. https://doi.org/10.1007/s10346-010-0203-2.

Soeters R, van Westen CJ. 1996. Slope instability recognition, analysis and zonation. Landslides, investigation and mitigation. *Transportation Research Board, National Research Council, Special Report* **247**: 129–177.

Stark CP, Guzzetti F. 2009. Landslide rupture and the probability distribution of mobilized debris volumes. *Journal of Geophysical Research: Earth Surface* **114**: F00A02. https://doi.org/10.1029/2008JF001008.

Stark CP, Hovius N. 2001. The characterization of landslide size distributions. *Geophysical Research Letters* **28**: 1091–1094. https://doi.org/10.1029/2000GL008527.

Sugai T, Ohmori H, Hirano M. 1995. Rock control on magnitude-frequency distribution of landslide. *International Journal of Rock Mechanics and Mining Sciences and Geomechanics Abstracts* **116A**.

Suzuki K. 1979. On the Disaster Situation/Land Condition Map of the Izu-Oshima Kinkai Earthquake, 1978. *Journal of the Japan Cartographers Association* **17**(2): 16–22. https://doi.org/10.11212/jjca1963.17.2_16.

Tang C, Westen CJV, Tanyaş H, Jetten VG. 2016. Analyzing post-earthquake landslide activity using multi-temporal landslide inventories near the epicentral area of the 2008 Wenchuan earthquake. *Natural Hazards and Earth System Sciences* **16**(12): 2641. https://doi.org/10.5194/nhess-16-2641-2016.

Tanyaş H, Allstadt KE, van Westen CJ. 2018. An updated method for estimating landslide-event magnitude. *Earth Surface Processes and Landforms* **43**: 1836–1847. https://doi.org/10.1002/esp.4359.

Tanyaş H, van Westen CJ, Allstadt KE, M.A. JN, Gorum T, Jibson RW, Godt JW, Sato HP, Schmidt RG, Marc O, Hovius N. 2017. Presentation and Analysis of a World-Wide Database of Earthquake-Induced Landslide Inventories. *Journal of Geophysical Research: Earth Surface* **122**: 1991–2015. https://doi.org/10.1002/2017JF004236.

Terzaghi K. 1962. Stability of steep slopes on hard unweathered rock. *Geotechnique* **12**: 251–270.

Tian YY, Xu C, Xu XW, Wu SE, Chen J. 2015. Spatial distribution analysis of coseismic and pre-earthquake landslides triggered by the 2014 Ludian MS6.5 earthquake. *Dizhen Dizhi* **37**: 291–306. https://doi.org/10.3969/j.issn.0253-4967.2015.01.023.

Uchida T, Kataoka S, Iwao T, Matsuo O, Terada H, Nakano Y, Sugiura N, Osanai N. 2004. A study on methodology for assessing the potential of slope failures during earthquakes. Technical Note of National Institute for Land and Infrastructure Management, No.204. http://www.nilim.go.jp/lab/bcg/siryou/tnn/tnn0204.htm (in Japanese with English abstract):

Van Den Eeckhaut M, Poesen J, Govers G, Verstraeten G, Demoulin A. 2007. Characteristics of the size distribution of recent and historical landslides in a populated hilly region. *Earth and Planetary Science Letters* **256**: 588–603. https://doi.org/10.1016/j.epsl.2007.01.040.

Wartman J, Dunham L, Tiwari B, Pradel D. 2013. Landslides in eastern Honshu induced by the 2011 Tohoku earthquake. *Bulletin of the Seismological Society of America* **103**: 1503–1521. https://doi.org/10.1785/0120120128.

Williams JG, Rosser NJ, Hardy RJ, Brain MJ, Afana AA. 2018. Optimising 4-D surface change detection: an approach for capturing rockfall magnitude–frequency distribution. *Earth Surface Dynamics* **6**: 101–119. https://doi.org/10.5194/esurf-6-101-2018.

Xu C, Xu X, Shyu JBH. 2015. Database and spatial distribution of landslides triggered by the Lushan, China Mw 6.6 earthquake of 20 April 2013. *Geomorphology* **248**: 77–92. https://doi.org/10.1016/j.geomorph.2015.07.002.

Xu C, Xu X, Shyu JBH, Zheng W, Min W. 2014a. Landslides triggered by the 22 July 2013 Minxian–Zhangxian, China, Mw 5.9 earthquake: Inventory compiling and spatial distribution analysis. *Journal of Asian Earth Sciences* **92**: 125–142. https://doi.org/10.1016/j.jseaes.2014.06.014.

Xu C, Xu X, Yao X, Dai F. 2014b. Three (nearly) complete inventories of landslides triggered by the May 12, 2008 Wenchuan Mw 7.9 earthquake of China and their spatial distribution statistical analysis. *Landslides* **11**: 441–461. https://doi.org/10.1007/s10346-013-0404-6.

Xu C, Xu X, Yu G. 2013. Landslides triggered by slipping-fault-generated earthquake on a plateau: an example of the 14 April 2010, Ms 7.1, Yushu, China earthquake. *Landslides* **10**: 421–431. https://doi.org/10.1007/s10346-012-0340-x.

Yagi H, Sato G, Higaki D, Yamamoto M, Yamasaki T. 2009. Distribution and characteristics of landslides induced by the Iwate–Miyagi Nairiku Earthquake in 2008 in Tohoku District, Northeast Japan. *Landslides* **6**: 335–344. https://doi.org/10.1007/s10346-009-0182-3.

Yagi H, Yamasaki T, Atsumi M. 2007. GIS analysis on geomorphological features and soil mechanical implication of landslides caused by 2004 Niigata Chuetsu earthquake. *Journal of the Japan Landslide Society* **43**: 294–306. https://doi.org/10.3313/jls.43.294.

Zhang J, Liu R, Deng W, Khanal NR, Gurung DR, Murthy MSR, Wahid S. 2016. Characteristics of landslide in Koshi River Basin, Central Himalaya. *Journal of Mountain Science* **13**(10): 1711–1722. https://doi.org/10.1007/s11629-016-4017-0.

Supporting Information

Additional supporting information may be found online in the Supporting Information section at the end of the article.

Figure S1. Estimated number for theoretically missing landslides in each inventory (Inventory IDs listed in Table 1).

Figure S2. Graphs showing the relation between (a) the rollover and (b) the cutoff values in relation to drainage density of landslide effected areas in each inventory.

Figure S3. FADs of inventories produced for the same earthquakes with the extent of the corresponding inventories' mapped areas and the trimmed versions of them for the common areas. TLA: Total landslide area (km2), TNL: Total number of landslides, OAI: Overlapping areas of inventories. *Because the inventory of Xu et al. (2015) is a point-based inventory, the overlapping area for this inventory set cannot be calculated.

Figure S4. Schematic drawing showing different hypothetical stages of the landslide initiation process: (a) small slides are triggered making a initiating larger landslide that will be formed in the next stage; (b) a larger slide is triggered, and it decreases the stability of entire slope; tension cracks and some other new small slides form; (c) slides of various sizes are triggered; they coalesce and form a larger body, but the overall slope remains unstable; and (d) many other slides are triggered, which cover the previously triggered landslides; they form an even larger final landslide geometry, until the slope reaches a stable state. Dashed black lines represent the final landslide geometry; red lines show newly triggered landslides in each stage; and blue lines show tension cracks.

Figure S5. Schematic drawing showing (a) progressive and (b) retrogressive failure. In both sections, 1 refers to initial failure and 2 shows the slope after movement of the surface rupture (adapted from (Cruden, 1993)).

Figure S6. Relation between the percentage of landslide population having areas larger than 1,000 m2, 2,500 m2, and 5,000 m2 and the location of the rollover and cutoff points.